River bank erosion and lateral accretion linked to hydrograph recession and flood duration in a mountainous snowmelt-dominated system

Nicholas A Sutfin[1*], Joel Rowland[1], Mulu Fratkin[1], Sophie Stauffer[1], Rosemary W.H. Carroll[2], Wendy Brown[3], Kenneth H. Williams[3,4]

[1]Earth and Environmental Sciences Division, Los Alamos National Laboratory, Los Alamos, NM
[2]Division of Hydrologic Sciences, Desert Research Institute, Reno, NV
[3]Rocky Mountain Biological Laboratory, Gothic, CO
[4]Lawrence Berkeley National Laboratory, Berkeley, CA
***** Current affiliation: Dept. of Earth, Environmental, and Planetary Sciences, Case Western Reserve University, Cleveland, OH

Corresponding authors: Nicholas A. Sutfin (Nicholas.sutfin@case.edu), Joel Rowland (jrowland@lanl.gov)

Key Points:

- Floodplain erosion and accretion estimated over 60 years using aerial lidar, repeat aerial imagery, field surveys, and historic flow data
- Hydrograph recession and duration of floodplain inundation explain 91% and 59% of the variability in bank erosion and lateral accretion
- Results can inform potential response to shifting climatic conditions and hydrologic regimes of snowmelt-dominated rivers

Abstract

Observed and projected global changes in the magnitude and frequency of river flows have potential to alter sediment dynamics in rivers, but the direction of these changes is uncertain. Linking changes in bank erosion and floodplain deposition to hydrology is necessary to understand how rivers will adjust to changes in hydrologic flow regime induced by increasing societal pressures and increased variability of climatic conditions. We present analysis based on aerial imagery, an aerial lidar dataset, intensive field surveys, and spatial analysis to quantify bank erosion, lateral accretion, floodplain overbank deposition, and a floodplain sediment budget in an 11-km long study segment of the meandering East River, Colorado, USA, over 60 years. Assuming steady state conditions over the study period, our measurements of erosion and lateral accretion close the sediment budget for a smaller 2-km long intensive study reach. We analyzed channel morphometry and snowmelt-dominated annual hydrologic indices in this mountainous system to identify factors influencing erosion and deposition in nine study sub-reaches. Results indicate channel sinuosity is an important predictor for both lateral erosion and accretion. Examination of only hydrologic indices across the study segment regardless of sub-reach morphology, indicate that the duration of flow exceeding baseflow and the slope of the annual recession limb explain 59% and 91% of the variability in lateral accretion and erosion, respectively. This work provides insight into hydrologic indices likely to influence erosion and sedimentation of rivers and reservoirs under a shifting climate and hydrologic flow regimes in snowmelt-dominated systems.

Plain Language Summary

Changing climatic conditions are poised to alter the timing and magnitude of precipitation, snowpack, snowmelt and the balance of water and sediment within river corridors. Understanding how these changes affect the stability of land along rivers is important for securing infrastructure, maintaining healthy ecosystems, preserving water quality, and understanding the fate and transport of contaminated sediment. This research uses aerial imagery, laser topographic scanning technology, field measurements of water and soil, and historical river flow data to examine linkages between river flows and erosion and deposition of sediment along the floodplain of a mountain over 60 years. Results show that river bank erosion is linked to the rate at which the river flows decrease following snowmelt-driven peaks and that the amount of sediment that is deposited along the river banks is linked to the duration of flooding; both are influenced by channel sinuosity. These results have important implications for understanding how rivers and freshwater resources may be impacted by shifting climatic conditions and hydrologic regimes.

1 Introduction

A large number of studies have quantified long-term channel migration and episodic bank erosion, but these approaches do not fully examine the link between changes in river flows and the timing of river bank erosion, particularly in snowmelt-dominated systems. Rapid changes in river flows likely strongly influence river bank stability and erosion on seasonal scales (Wolman, 1959; Simon et al., 2002). Annual hydrologic trends including the magnitude, frequency, timing, duration, and rate of change in discharge are important aspects of river flow regimes that influence aquatic and riparian habitat (Poff et al., 1997) and sediment dynamics including erosion and deposition along floodplains (Wohl et al., 2015). More specific investigation of hydrologic

flow regimes have been examined using various hydrologic indices to provide insight into riverine ecosystems (Richter et al., 1996) and germination of riparian vegetation (Benjankar et al., 2014; Caponi et al., 2019). These changes that characterize annual hydrologic flow regimes across all climatic zones can include very rapid changes in discharge, such as those in flashy rainfall dominated systems. Alteration of natural flow regimes induced by dams and flow regulation – common in snowmelt dominated systems – can mimic these rapid changes and greatly alter sediment regimes and riverine habitat (Richter et al., 1996; Poff et al., 1997; Lenhart et al., 2013).

While understanding the mechanisms and timing of bank erosion is fundamental to landscape evolution and risk to infrastructure, it is also crucial for nutrient and carbon dynamics and potential impact to water resources. The rate at which banks erode and rivers migrate substantially influence nutrient and carbon dynamics (Sekely et al., 2002; Sutfin et al., 2016), ecosystem habitat (Naiman et al., 2010), and the fate and transport of contaminants bound to floodplain sediment (Macklin et al., 2006; Rhoades et al., 2009). Changes in erosion and deposition along floodplains can greatly alter carbon storage along floodplains (Noe & Hupp, 2005; Hoffmann et al., 2009; Omengo et al., 2018; Scott & Wohl, 2018; Lininger et al., 2019), which is substantially higher within snowmelt-dominated mountainous headwater systems (Wohl et al., 2012; Sutfin et al., 2016; Sutfin & Wohl, 2017). Contaminants adsorbed to mineral facies and organic matter in floodplain and bank sediment of mountain streams, such as the heavy metals from the mining spill along the Animas River in Colorado, USA, (Rodriguez-Freire et al., 2016), are susceptible to erosion and pose a risk for downstream water quality and ecosystems. The research presented here is motivated by our efforts to quantify carbon storage and dynamics in a mountainous region along the floodplain of the East River near Crested Butte, Colorado, USA. The general goals of this research were to quantify

103 erosion and deposition along the East River and to link these observations to past
104 hydrologic conditions.

105 Many researchers have used remotely sensed imagery to examine bank erosion
106 and lateral accretion over years to decades (James E. Pizzuto, 1994; Micheli & Kirchner,
107 2002a, 2002b; S. S. Day et al., 2013b, 2013a; Lenhart et al., 2013; Rowland et al., 2016;
108 Schook et al., 2017; Schwenk et al., 2017; Caponi et al., 2019). Using these data as a
109 basis for understanding river migration rates, modeling efforts seek to understand the
110 physically-based drivers of channel migration over long time scales (i.e., 10^2 to 10^5
111 years) (Howard, 1996; Güneralp & Rhoads, 2009; G. Parker et al., 2011; Bogoni et al.,
112 2017), or use near-bank velocities to estimate bank erosion over shorter time scales
113 (Darby et al., 2007; Gary Parker et al., 1982; J. E. Pizzuto & Meckelnburg, 1989).

114 Physically based models of bank erosion provide understanding of cantilever
115 failures, slip or rotational failures, and planar shear resulting from undercutting, positive
116 pore pressure, and excess bank shear stress, respectively (Thorne & Tovey, 1981;
117 Simon et al., 2000; Langendoen & Simon, 2008; Langendoen & Alonso, 2008). Available
118 models tend to use bankfull flow conditions to model bank erosion (Langendoen &
119 Alonso, 2008) and past work indicates that more erosion is likely to occur at high flow
120 conditions. However, changes in flow have also been identified as potential drivers for
121 bank failure because positive pore pressure of saturated banks combined with the loss
122 of supporting pressure when stage declines make slip and rotational bank failures likely
123 (Rinaldi & Casagli, 1999). Thus, additional hydrologic indices such as the rate of change
124 offer the potential to provide a more robust understanding of the hydrologic drivers of
125 bank erosion.

126 Effectively linking floodplain erosion and accretion to hydrology requires the
127 assumption of minimal changes in sediment supply and are simplified by the assumption

of steady state and a balanced sediment budget over the time period examined. Sediment budgets at the watershed scale must consider the production of sediment from weathering and erosion, elements of storage within the basin, sediment transport processes, and the resulting sediment yield (Dietrich et al., 1982; Gellis & Walling, 2013). Sediment budgets for only floodplains, however, may be simplified needing only to account for the time averaged balance of erosion and deposition along the floodplain alone (Reid & Dunne, 2016). Examples of floodplain sediment accounting includes those in the southwestern United States by Gellis et al. (2012) and in the Le Sueur watershed in Minnesota, USA, by Belmont et al., (2011) and Day et al., (2013). Here, we use a floodplain sediment budget to constrain estimates of floodplain erosion and sedimentation along a subalpine meandering river using a combination of field observations, remotely sensed imagery and lidar, and GIS spatial analysis.

We studied the connections between hydrology and sediment flux of the East River floodplain, using (1) repeat aerial imagery to quantify lateral erosion and accretion over a 60-year period, (2) measurement of floodplain fine sediment depth, (3) an aerial lidar digital elevation model (DEM) and (4) empirical relationships with characteristics of the flow regime to identify hydrologic drivers of river bank erosion and lateral accretion. From this work, we developed an empirical relationship between hydrology and sediment fluxes on decadal time scales to address the primary goal to determine what morphometric variables (e.g., sinuosity, channel slope, width) and hydrologic indices (e.g., peak magnitude, timing of peak, slope of the recession limb) best explain observed floodplain erosion and accretion on the snowmelt-dominated East River. We also calculated a sediment budget to verify our accounting of eroded and accreted floodplain sediment and used the results to examine a practical and cost-effective way to estimate

hydrologic influence on floodplain erosion and accretion that does not require the intensive fieldwork and lidar analysis employed in this study.

2 Study Area

We studied an 11-km long segment of the East River approximately 3.5 km down valley from Gothic, CO, (Figure 1) near Crested Butte. At the downstream end of the study segment, the East River drains approximately 134 km^2 and has an annual average precipitation of 64 cm (SNOTEL, 2017). The floodplain lies directly downstream of steep, confined, mountainous tributaries that incise through sandstones, mudstones, shales, granodiorite and metamorphosed byproducts of the uplifted White Rock pluton in the Elk Mountains of Colorado (Gaskill et al., 1991). Within the floodplain reach, the East River is a gravel-cobble bed, sinuous alluvial river approximately 20-m wide on average and bounded by lateral Pinedale glacial moraines, landslide deposits, and outcrops of Mancos Shale along the bed and valley walls. Sedges, grasses, and willows dominate the vegetation along the floodplain with isolated trees, dominantly blue spruce, scattered along the reach, but rarely located along the river banks. Throughout the floodplain, extensive beaver activity results in dams, lodges and the introduction of large wood from the surrounding hillslopes. Floodplain fine overbank sediment is dominated by silt-size particles with varying proportions of sand, clay, and minimal gravel content (Malenda et al., 2019). Beneath fine sediment, the floodplain is composed of gravel and cobbles, and contains lenses of finer, sorted material. Erosion of underlying gravels and undercutting of fine overbank sediment commonly result in cantilever failure of grass-covered blocks along the East River 11-km long study segment (Figure 1D, S1).

The East River is a typical snowmelt-dominated system, which is characterized by a gradual rising limb as temperatures warm and snow melts in the spring months of

April and May. An annual peak flow commonly occurs in the latter half of May or early half of June after peak snowmelt, followed by a gradual recession limb that takes place over weeks to months at which discharge returns to some baseflow condition sometime between September and November.

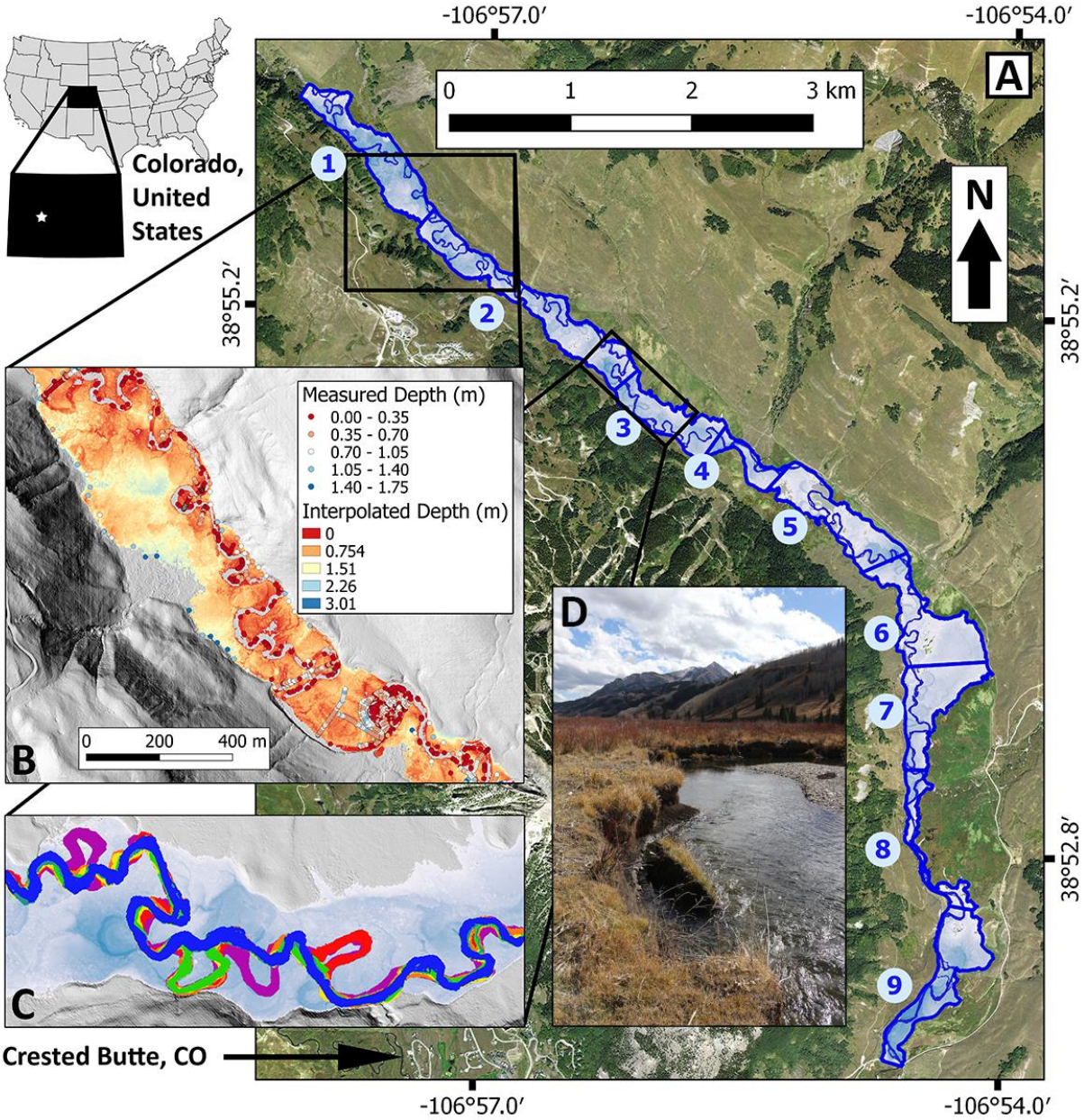

Figure 1. Map of study area on the East River near Crested Butte, Colorado, USA. The floodplain was delineated by "flooding" a 0.5-m resolution lidar digital elevation model along the 11-km long study segment, which was divided into 9 study reaches (A) based on changes in valley slope. The depth of fine sediment was measured across the floodplain at 1847 points and interpolated across the upper 2 km, intensive study reach

(B) consisting of reach 1 and approximately half of reach 2, ending at the downstream extent of the black box in (A). Masks of the river channel, depicted in various colors, were derived for all seven time periods (C), and used to determine lateral accretion and erosion, typically occurring as cantilever failures in the study area (D). Shades of blue indicate relative depth of water across the delineated floodplain in A and C.

Limited land-use impacts have influenced the watershed upstream of the 11-km long study segment of the East River. From 1880 to 1890, a silver mine operated along Copper Creek upstream of Gothic, CO, the present location of the Rocky Mountain Biological Laboratory. The mining area is now designated as US Forest Service (USFS) national forest and wilderness area. Land use along the 11-km long study segment consists of small privately owned parcels and U.S. Forest Service (USFS) land, on which ranchers graze cattle for limited portions of the year (Theobald et al., 1996). Limited property access restricted our field investigations to the upper 2 km, intensive study reach (Figure 1A; Reach 1 and half of reach 2). Although flow diversions exist within the 11-km long study segment, they were present prior to beginning of the study period in 1955 and they primarily capture runoff from tributaries before they reach the East River.

3 Materials and Methods

Spatial analysis of aerial lidar, repeat aerial imagery, surface water flow measurements and historical hydrologic flow analysis, measurements of floodplain fine sediment depth, and multiple linear regression were used to examine linkages between hydrology and bank erosion, accretion, and channel migration rates over 60 years.

3.1 Terrain Analysis and Study Reach Delineation

Aerial lidar was collected in August of 2015 for the entire East River watershed. Average bare-ground point cloud density of lidar was 4.29 points/m^2 resulting in a total accuracy with root mean squared error of 0.05 m at the 95% confidence level. A hydro-flattened, bare-ground DEM with a horizontal resolution of 0.5 m derived from the lidar

point cloud data was used for all topographic analysis. Using the valley slope, we divided the ~11-km long floodplain segment into nine study reaches. We calculated the valley slope using a best-fit line of elevation points extracted from the 2015 DEM and spaced every 10 meters down the valley center. We detrended the slope of the 9 sub-reaches using the raster calculator in QGIS and recombined them to generate a floodplain DEM with zero down-valley slope and a maximum total relief of 5.44 m. We artificially entrenched the flat lidar water surface by 2 meters and used the *r.fill.dir* Grass tool in QGIS to flood the detrended DEM at a depth of six meters to delineate the approximate extent of the floodplain. We verified the digitally delineated floodplain extent with field observations of distinct breaks in slope, such as the base of lateral moraines, toes of alluvial fans, and abutments to incised bedrock outcrops.

3.2 Channel Position and Movement using Aerial Imagery

We used aerial images from seven dates (i.e., 1955, 1973, 1983, 1990, 2001, 2012, 2015) obtained from the US Geological Survey, US Department of Agriculture, and the US Forest Service to delineate the channel, measure channel widths, sinuosity, and lateral erosion and accretion over time. All imagery was resampled to 1-m resolution to allow direct comparison between images. We georeferenced the 2015 imagery using the 2015 lidar DEM dataset as a reference using >6 control points including the corners of buildings, intersections of roads and fences, and the base of mature trees. All other images were georeferenced (if not already done so by the source agency) through comparison with similar point types in the 2015 georeferenced image.

To analyze channel characteristics and compare changes over time, we generated binary channel masks for each set of aerial imagery. For color imagery between 1973 and 2015, we generated masks of bankfull river extent using red-green-blue (RGB) color bands and the normalized difference water index (NDWI) to classify the

channel water surface in each image (Figure 1C; McFeeters, 1996) using the object-oriented classification software, eCognition. To control for variations in water levels between images, regions of tan and grey gravel and sand bars devoid of vegetation and exposed, un-vegetated bank faces were included in the channel mask as an estimate of bankfull extent (Gurnell, 1997; Richard et al., 2005; Mount & Louis, 2005; Fisher et al., 2013; Rowland et al., 2016; Donovan et al., 2019). The black and white 1955 USDA photos required manual delineation of the channel mask.

Metrics calculated to quantify the channel and floodplain attributes for the nine valley reaches and entire 11-km long study segment included: valley, floodplain, and channel areas; valley and channel lengths; elevation change along the reach; valley and channel slopes; sinuosity; average channel width; and valley confinement. The channel area relative to the area of delineated valley floor defined valley confinement as a proxy for potential of the floodplain to accommodate channel migration, dissipate energy during overbank flow, and facilitate overbank deposition. Channel sinuosity measures the channel length divided by the straight down-valley length. Channel slope was calculated as the valley slope divided by channel sinuosity. Channel width, linear erosion, and accretion rates were determined for each bank pixel using the Spatially Continuous Riverbank Erosion and Accretion Measurements algorithm (SCREAM; Rowland et al., 2016).

Linear rates represent the distance that a river bank face moves in a given time interval by measuring the Euclidean distance between a bank pixel in one river mask and the closest bank pixel at the subsequent river mask. Eroded and accreted floodplain areas derived from SCREAM were divided by the number of years within that time period and the channel length to estimate linear rates of erosion and accretion. Three sources of error are associated with our measurements of linear change: image

registration, image classification and the accuracy of SCREAM output (Rowland et al., 2016). Average estimated registration error for the 1-m imagery from 1973 to 2015 was 0.58 m. Poor image quality of the 1955 photographs prevented direct estimates of error using this method, so we have assigned a registration error equal to two times the highest error (1.2 m) in areas for the period between 1955-1973. Errors associated with area-based erosion and accretion measurements as a result of image mis-registration for each time period were assigned as percentage of change in areas following the methodology detailed in Rowland et al. (2016). Total measurement errors were estimated by combining registration, classification, and methodological errors in quadrature (Rowland et al. 2016)) (Table S1).

3.3 Vertical Accretion Rates

We estimated long-term vertical accretion rates using a combination of field-based measurements of fine-grained deposit thickness and changes in channel position from aerial imagery between 1973 and 2015. Images from 1955 were excluded from this analysis because of the uncertainty associated with the poor-quality images. In 2016, along the upper 2 km, intensive study reach (Figure 1A, reach 1 and half of reach 2), we measured thickness of fine-grained deposits at 324 locations on 21 transects by inserting a soil probe into the floodplain surface until refusal at bedrock or gravel-size material (>2mm). Mean migration rate was estimated from SCREAM output and the distance to each transect point from the channel was converted into duration since channel occupation by dividing by the bend averaged migration rate (Figure S2). More detailed analysis to examine vertical accretion rates in conjunction with the channel migration rate over each time period was conducted and outlined in the supplemental information (Figure S2), but suspected point bar erosion did not produce robust results that support continuous vertical accretion for each time period. Instead, we used the total

depth to represent an average deposition rate over the time period examined. The measured depth of fine sediment (d_i) was then divided by the duration since occupation by the river channel (t_i, when fine sediment depth would have been equal to zero) to estimate a mean vertical accretion rate (a_i; Equation 1).

$$\overline{a_i} = \frac{d_i}{t_i} \quad (1)$$

Potential predictors of floodplain vertical accretion rates, across the upper 2 km, intensive study reach were assessed through stepwise multiple linear regression. Variables examined for this analysis were similar to those described above, with the following additions. Distance from the channel was measured in the field. Relative elevation from the bankfull stage at the transect was extracted from the lidar at the top of point bars were bar sand/gravel transitioned into vegetation cover. Along each transect, channel width, valley width, and the ratio between the two (valley confinement) were measured from the imagery in GIS. Localized valley slope, channel slope, and sinuosity were measured using GIS extending approximately 50 m upstream to 50 m downstream of the transect. Mean values of radius of curvature, lateral accretion rate, and erosion rate were calculated along each meander bend. Measurements were denoted as either being on the inside or outside of a bend. The angle of each transect was used as a proxy for the angle of each river bend relative to the down valley direction from 0-90º.

3.4 Estimating floodplain sediment volumes

Areas of accretion and deposition from the SCREAM analysis were converted to sediment volumes using measured sediment depths. In our analysis, we only estimate volumes of fine grained (less ~ 2mm in grain diameter) sediments deposited on top of the gravel-rich channel and point bar deposits. In addition to the soil probe measurements collected on point bar transects (Section 3.3), 1,587 measurements were

made along the upper 2 km intensive study reach (Figure 1A, Reaches 1 and 2; Sutfin & Rowland, 2019). We subtracted these depth measurements from the DEM elevations using the *raster calculator* in QGIS to calculate an absolute elevation of underlying gravel/bedrock. We then generated a triangular irregular network (TIN) of the gravel/bedrock surface elevation using the *interpolate* tool in QGIS. By subtracting elevations of this interpolated surface from the ground surface elevations, we created a spatially continuous isopach map of fine-grained floodplain sediment.

This interpolated fine-sediment map represents conditions in 2015. At the location of the current channel the fine sediment has values of zero, as such, areas of historical floodplain erosion that intersected the 2015 channel did not have accurate values of the floodplain volume eroded. To correct for this error we interpolated 2015 fine-sediment thickness across the channel using a 3 m buffer that extended beyond the locally thin deposits covering active point bars. We used the *close gap* Saga tool in QGIS (threshold = 0.1) to create the corrected isopach map. We calculated eroded volumes by multiplying the areas of eroded regions derived from the aerial imagery for each time interval by the interpolated isopach map of fine sediment within those mapped areas.

Using the estimated vertical accretion rates from our soil probe transects we estimated an average deposition rate for laterally accreted regions along the channel and developed a multiple linear regression model to estimate overbank deposition on the stable floodplain surface in response to floods. For the laterally accreted areas, we used the average migration rates at the bends determined using the probe transects described above in section 3.3 to determine the portion of contemporary floodplain that would have been formed by lateral accretion during the 42 years between 1973 and 2015. A reach-based average migration rate and resulting mean migration distance

along the probe transects were used to estimate an average vertical accretion rate from all points within the mean migration distance for the entire period between 1973-2015 (Table S2). This average rate was multiplied by the mapped accretion areas from the aerial photos and SCREAM output to provide a volume of laterally accreted sediments.

Overbank deposition rates beyond 10 m were calculated for each cell utilizing another multiple linear regression model including only the two strongest predictor variables, distance from the channel and relative elevation from the channel (Figure S3). The *proximity grid* Saga tool in QGIS was used to create a grid based on distance from the channel for images from the six years. Floodplain elevation relative to the channel was calculated by subtracting the minimum elevation from the detrended 2015 DEM floodplain surface (derivation described above in section 3.1). This assigned a relative elevation to every raster pixel. The river channel buffered by three meters on both sides was subtracted from the relative elevation grid and the *close gap* tool in QGIS was used to interpolate elevations across the channel.

The distance-from-channel raster and the detrended-valley DEM were used as input to the vertical accretion rate regression model equation in the raster calculator to generate raster grids of estimated overbank deposition rates for all six time periods. Overbank sediment deposition estimates of volume were made by multiplying calculated rates by the number of years in the respective time interval, summing all pixel values for each period, and multiply that value by the area of each pixel (0.25 m^2). Vertical accretion within abandoned channels was estimated using the lateral accretion rate of 3.3 cm y^{-1} within the first 10 m from the channel for periods following cutoff occurrence. Aggradation of previously abandoned channels was based on the relative vertical and horizontal distance from the active bankfull channel at distances exceeding 10 m. Rates

of volume of sediment accreted and eroded during each time period were estimated by dividing the total volume of sediment by the number of years in each time period.

3.5 Streamflow Data and Hydrologic Analysis

Streamflow was measured 22 times near the Crested Butte city water pump house in the upper 2 km, intensive study reach, from October, 1st, 2014, to September, 30th, 2017, and a stage-discharge rating curve was created against stage data recorded every 15 minutes (r^2 = 0.99) (Carroll & Williams, 2019). To extend the flow record prior to 2014, we regressed measured discharge at the 2-km intensive study reach against data from the US Geological Survey stream gage on the East River at Almont (gage # 09112500) 40 km downstream (r^2 = 0.97; Figure 3A). Using this regression, we generated a synthetic hydrograph for the study site from 1934-2018 using the Almont streamflow data (Table S3). A comparison of the synthetic hydrograph and flows measured between 2014 and 2018 showed a strong agreement with a Nash-Sutcliffe Efficiency coefficient (NSE) of 0.97 (Figure 3B). Flow frequency analysis was conducted on the entire synthetic hydrograph to determine annual statistics for the continuous 82 years. Analysis of possible hydrological drivers for erosion and deposition examined the synthetic hydrograph from 1955 to 2015 to correspond with the aerial imagery analysis.

We used R software (R Core Team, 2017) to extract synthetic hydrograph characteristic between 1955 and 2015. An average minimum flow value of 0.49 m^3 s^{-1} during the low-flow months of October, November, December, January, February, and March were used as a reference baseflow condition. Bankfull flow was estimated as 8 m^3 s-1 based on field observations and hydrologic analysis indicates an approximate recurrence interval of 1.2 years. The mean value for the day of the year on which peak flow occurred, the last day exceeding bankfull flow conditions, and the last day exceeding baseflow conditions were calculated for each time period. The maximum and

mean values within each time period were calculated for annual hydrograph peak magnitude, peak timing, annual volume of discharge, the annual volume of water above bankfull flow, duration between the first and last day of flow exceeding baseflow, the number of days on which baseflow occurred, the annual volume of discharge exceeding bankfull, duration between the first and last day of flow exceeding bankfull flow, the number of days on which bankfull flow occurred, and the cumulative number of days since the last bankfull flow, the total recession limb slope from the annual maximum peak to baseflow, the bankfull recession limb slope from bankfull stage to baseflow, and the number of peaks above bankfull flow. Recession slopes were estimated as the slope of the line between peak discharge and the first occurrence of baseflow conditions.

A secondary analysis was conducted to examine diel fluctuations in discharge associated with the slope of the recession limb of each annual hydrograph. A regression analysis of 15-minute streamflow data from the same USGS gauge and measured flow at the study site from 2015-2019 yielded an $r^2 = 0.94$. This regression was used to extend the study site discharge data to span the duration of the 15-minute data from 1988-2019. Maximum and minimum daily values were determined using hourly data and the number and magnitude of diel fluctuations exceeding 6 m^3s^{-1} within a window of 5 to 10 m^3s^{-1} were summed. Correlations were examined between the recession limb slope and the number, the summed magnitude, and the average magnitude of diel fluctuations to occur within the defined recession window.

3.6 Statistical Analyses

The number of potential variables for all multivariate regression models used to identify significant predictors was reduced to minimize collinearity of predictor variables prior to multiple linear regression. Starting with the most strongly correlated variable and working sequentially through variables with decreasing correlation values, variables were

412 eliminated as potential predictors for the regression model if they were moderately cross
413 correlated ($r > 0.7$) with another more strongly correlated variable (Dormann et al., 2013)
414 already selected as a predictor. Stepwise multiple linear regression was conducted
415 using the *stats* package *lm* function in R statistical software to examine possible
416 predictor variables and determine the best regression model for: (1) the area of accreted
417 and (2) the area of eroded floodplain along nine study reaches, and (3) vertical
418 floodplain deposition rate estimated from measurements of floodplain fine sediment
419 depth along the upper 2 km, intensive study reach over the 6 time periods. Multiple
420 linear regression assumptions of normality and homoscedasticity of model residuals
421 were met with power transformations and verified using the Shapiro-Wilk normality test
422 (*shapiro.test* function) and the non-constant error variance test in R (*ncv.test* function),
423 for which details are provided in supporting material. Variables were included in stepwise
424 multiple linear regression to identify the best regression model based on minimizing the
425 Akaike Information Criteria (AIC).

426 **4. Results**

427 *4.1 Channel and floodplain metrics*

428 The floodplain delineation of the entire 11-km long study segment resulted in a valley
429 bottom area of 2.65 km^2 with a total valley length of 10.62 km and a total valley slope of
430 0.64%. Despite the occurrence of 21 channel chute cutoffs in the 60-year time period,
431 channel slope and the sinuosity for the entire river segment remained relatively constant
432 during the six periods examined. Channel slope along the entire 11-km long study
433 segment varied from 0.34 to 0.36% over the 60-year time period. Sinuosity fluctuated
434 about a mean value of 1.81 ± 0.04 m/m (SD) with a minimum and maximum of 1.77 to
435 1.89 (Table 1).

Table 1. Morphological characteristics of the entire East River study segment derived from remotely sensed imagery and lidar for each time period. Channel width was calculated as a mean of channel width pixel values from SCREAM and standard deviations of those averages are provided following each mean.

Year	Floodplain area (km^2)	Channel Area (km^2)	Channel Length (km)	Sinuosity (m/m)	Channel slope (%)	Confinement (m^2/m^2)	Mean channel width (m)
1955	2193.6	459.0	20.08	1.89	0.339	0.17	25 ± 2
1973	2254.0	398.7	19.29	1.82	0.353	0.15	20 ± 2
1983	2222.3	430.3	18.80	1.77	0.362	0.16	23 ± 3
1990	2295.4	357.3	18.90	1.78	0.361	0.13	19 ± 3
2001	2275.4	377.3	19.39	1.83	0.352	0.14	21 ± 3
2011	2296.2	356.5	18.81	1.77	0.362	0.13	19 ± 1
2015	2312.2	340.4	18.98	1.79	0.359	0.13	17 ± 1

Table 2. Morphological characteristics of nine study reaches derived from remotely sensed imagery and lidar. Values are averaged from the seven images spanning 60 years and standard deviations of those averages are provided following each mean.

Reach	Valley area (m^2)	Valley Length (m)	Valley slope (%)	Floodplain area (m^2)	Channel Area (m2)	Channel Length (m)	Sinuosity (m/m)	Channel slope (%)	Confinement (m^2/m^2)	Channel width (m)
1	344236	1471	0.94	294462	49774 ± 6292	2860 ± 130	1.94 ± 0.09	0.48 ± 0.02	0.14 ± 0.02	18 ± 3
2	489119	2126	0.74	405784	83334 ± 6234	4735 ± 143	2.23 ± 0.07	0.33 ± 0.01	0.17 ± 0.01	18 ± 2
3	232658	910	0.55	199873	32785 ± 6046	1740 ± 99	1.91 ± 0.11	0.29 ± 0.02	0.14 ± 0.03	19 ± 3
4	93445	595	0.86	76134	17311 ± 1495	903 ± 60	1.52 ± 0.10	0.57 ± 0.04	0.19 ± 0.02	20 ± 2
5	330488	1142	0.68	283494	46994 ± 5334	2419 ± 170	2.12 ± 0.15	0.32 ± 0.02	0.14 ± 0.02	20 ± 2
6	378666	924	0.56	344169	34497 ±4194	1448 ± 248	1.57 ± 0.27	0.37 ± 0.06	0.09 ± 0.01	22 ± 3
7	302210	855	0.33	271371	30839 ± 6166	1490 ± 116	1.74 ± 0.14	0.19 ± 0.02	0.10 ± 0.02	21 ± 3
8	126101	1175	0.54	89108	36992 ± 2469	1583 ± 26	1.35 ± 0.02	0.40 ± 0.01	0.29 ± 0.02	23 ± 3
9	355743	1420	0.46	299779	55965 ± 8114	2001 ± 53	1.41 ± 0.04	0.33 ± 0.01	0.16 ± 0.02	23 ± 4

443 Valley slope ranged from 0.33% to 0.94% along each of the 9 delineated study reaches
444 with a mean of 0.36 ± 0.19% (SD; Table 2). Mean valley confinement for the time period was
445 0.16 ± 0.02 m^2/m^2 (mean ± SD). Study reach 8 is the most confined reach (C_v = 0.29 ± 0.02) and
446 is located toward the downstream end of the 11-km long study segment where the tributary
447 alluvial fan from Brush Creek constricts the East River valley. Reach sinuosity (P) averaged
448 over the time period is also lowest in study reach 8 at 1.35 ± 0.02 m/m (Figure 2). The highest
449 reach mean sinuosity (P = 2.23 ± 0.07) occurred in reach 2, which is moderately confined (C_v =
450 0.17 ± 0.01) (Table 2).

451 Averaged over all time periods, channel width generally increased from upstream
452 reaches to downstream reaches (Table 2). Although the channel mean width fluctuated with
453 intervals of widening followed by narrowing, there was a net overall decrease over the 60-year
454 time period. The average channel width for the entire 11-km long study segment decreased
455 from a high of 25 ± 2 m in 1955 to a minimum of 17 ± 1 m in 2015. The greatest width reduction
456 (~5 m) occurred between 1955 and 1973, but a substantial decreased of >4 m also occurred
457 during two time periods between 2001 and 2015.

458 *4.2 Channel Migration and Floodplain Area*

459 The net balance between total area of eroded and accreted floodplain by the East River
460 varied over the six time periods, with estimated accretion greater than erosion in four out of six
461 time periods (Table 3). Over the entire 60-year period accretion exceeded erosion by 120,036 **±**
462 43,973 m^2, equal to 5.3% of the total area of the valley bottom. This accretion total includes the
463 area of 21 abandoned channels arising from meander bend cutoffs. The highest rate of change
464 in floodplain sediment balance occurred from 1983-1990 with a mean accretion rate outpacing
465 erosion by a factor of four (Table 3; Figure 2). There was an observed decrease in channel
466 width during this period, followed by a period dominated by erosion and channel widening. The

period between 1973 and 1983 was dominated by the largest erosion rates observed in this study, and was accompanied by an observed increase in channel width (Table 1, 3; Figure 2A).

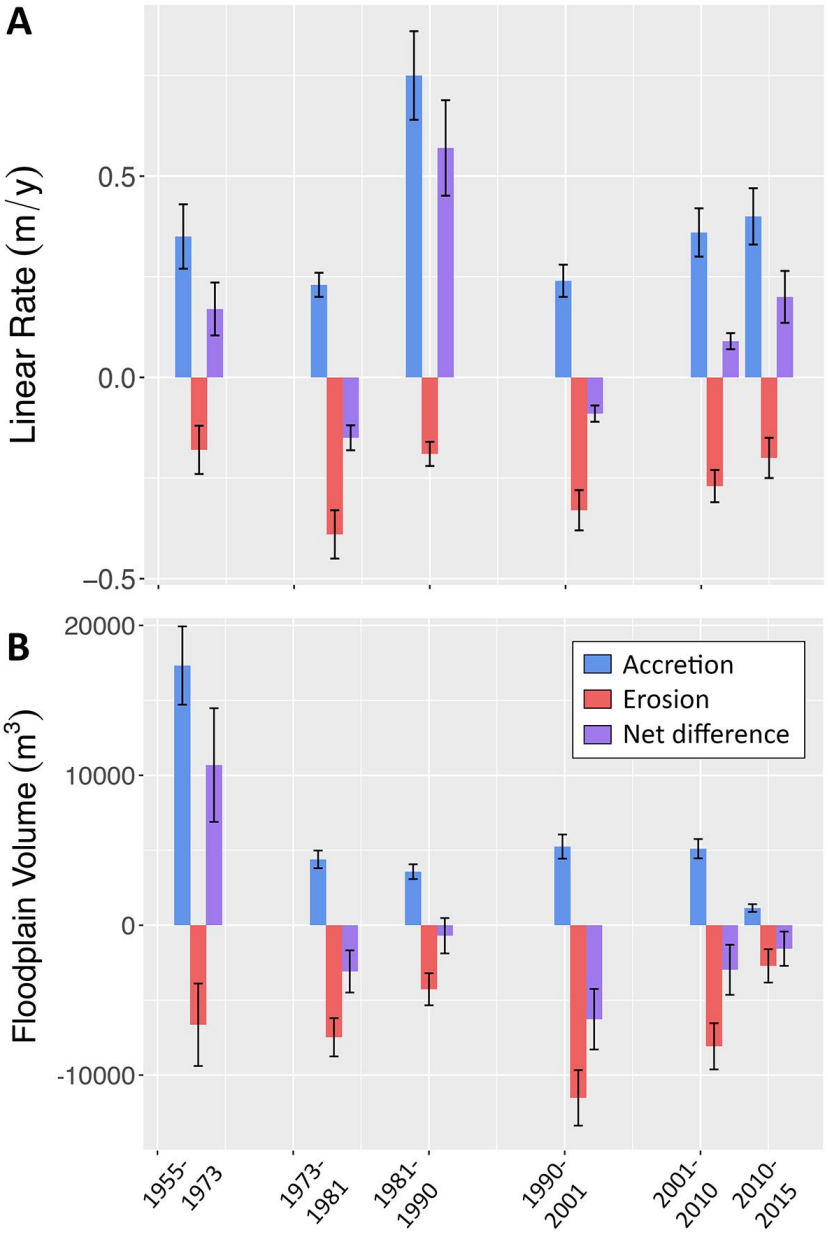

Figure 2 Bar plots of estimated accretion, erosion, and net difference (accretion minus erosion) in linear rates along the entire 11-km long study segment (A) and volume of floodplain fine sediment along the upper 2 km, intensive study reach (B) during each time period examined over the 60 year study period.

476 **Table 3.** Area accreted and eroded across the entire 11-km long study segment and hydrologic
477 flow indices on the East River during the six time periods of the study.

	1955-1973	1973-1983	1983-1990	1990-2001	2001-2011	2011-2015	Mean	Total
Duration (years)	18 ± 0.3	10 ± 0.3	7 ± 0.3	11 ± 0.3	10 ± 0.3	4 ± 0.3	10 ± 0.3	60 ± 0.8
Accretion (m^2)	125529 ± 27774	45276 ± 6339	99194 ± 13887	50226 ± 8036	70686 ± 9189	30156 ± 7539	70178 ± 12127	421067 ± 34789
Erosion (m^2)	-64915 ± 25388	-74670 ± 12694	-24569 ± 6142	-69550 ± 11128	-52358 ± 9948	-14969 ± 6137	-50172 ± 11906	-301031 ± 33224
Net Change (m^2)	60614 ± 37629	-29394 ± 14188	74625 ± 15185	-19324 ± 13726	18328 ± 13543	15187 ± 9721	20006 ± 17332	120036 ± 48106
Accretion Rate (m^2y^{-1})	6974 ± 1548	4528 ± 652	14171 ± 2095	4566 ± 744	7069 ± 949	7539 ± 1987	7474 ± 1329	44846 ± 3551
Erosion Rate (m^2y^{-1})	-3606 ± 1412	-7467 ± 1294	-3510 ± 893	-6323 ± 1030	-5236 ± 1010	-3742 ± 1566	-4981 ± 1201	-29884 ± 2999
Mean linear Accretion Rate ($m\ y^{-1}$)	0.347 ± 0.077	0.235 ± 0.034	0.754 ± 0.111	0.242 ± 0.039	0.365 ± 0.049	0.401 ± 0.106	0.390 ± 0.069	2.343 ± 0.186
Mean Linear Erosion Rate ($m\ y^{-1}$)	-0.180 ± 0.070	-0.387 ± 0.067	-0.187 ± 0.048	-0.334 ± 0.054	-0.270 ± 0.052	-0.199 ± 0.083	-0.259 ± 0.062	-1.557 ± 0.156
Mean Day of Peak Flow	152.7	162	156.3	151.5	147	155.3	154.13 ± 5.06	
Mean Peak Flow (m^3s^{-1})	11.84	11.6	12.9	12.35	11.31	10.15	11.69 ± 0.94	
Max Peak Flow (m^3s^{-1})	22.56	18.32	21.86	23.74	16.02	15.49	19.67 ± 3.53	
Mean Bankfull Duration (days)	31.3	38.1	41	36.1	29.3	25.5	33.55 ± 5.84	
Max Bankfull Duration (days)	61	48	64	63	47	31	52.33 ± 12.86	
Mean Days Above Bankfull Flow	20.3	24	22.6	23.8	18.5	12.8	20.33 ± 4.26	
Max Days Above Bankfull Flow	59	46	62	56	47	30	50.00 ± 11.71	
Mean Duration Above Baseflow (days)	215.5	218	255.1	230.9	263	278.5	243.50 ± 25.82	
Max Duration Above Baseflow (days)	362	331	364	305	364	349	345.83 ± 23.74	
Mean Days Above Baseflow	232.1	217.8	266.7	243.9	259.8	245.5	244.30 ± 17.86	
Max Days Above Baseflow	281	261	362	275	316	272	294.50 ± 37.97	
Mean Days Since Bankfull Flow	267	327.1	349.6	261.3	345.3	455.3	334.27 ± 70.58	
Max Days Since Bankfull Flow	925	904	935	579	944	901	864.67 ± 140.96	
Mean Day Baseflow Ends	280.2	288.6	304	305.3	291	321.3	298.40 ± 14.73	
Mean Day Bankfull Flow Ends	173.3	181.9	176.8	172.7	170.3	173	174.67 ± 4.11	
Mean No. Peaks Above Bankfull		1.9	2	1.8	1.4	0.5	1.52 ± 0.61	
Maximum No. Peaks Above Bankfull	3	4	5	4	3	1	3.33 ± 1.37	
Mean Total Recession Slope ($m^3\ s^{-1}\ day^{-1}$)	0.094	0.087	0.083	0.077	0.079	0.056	0.08 ± 0.01	
Max Total Recession Slope ($m^3\ s^{-1}\ day^{-1}$)	0.149	0.142	0.097	0.13	0.124	0.085	0.12 ± 0.03	
Mean Bankfull Recession Slope ($m^3\ s^{-1}\ day^{-1}$)	0.076	0.064	0.059	0.058	0.066	0.047	0.06 ± 0.01	
Max Bankfull Recession Slope ($m^3\ s^{-1}\ day^{-1}$)	0.12	0.086	0.082	0.075	0.091	0.05	0.08 ± 0.02	
Mean Total Annual Volume (km^3)	0.060	0.059	0.067	0.065	0.057	0.051	0.060 ± 0.006	
Max Total Annual Volume (km^3)	0.109	0.081	0.103	0.110	0.087	0.077	0.094 ± 0.015	
Mean Bankfull Volume (km^3)	0.027	0.034	0.037	0.033	0.027	0.024	0.031 ± 0.005	
Max Bankfull Volume (km^3)	0.074	0.047	0.072	0.073	0.050	0.031	0.058 ± 0.018	

478

479 *4.3 Floodplain Vertical Accretion*

Measured total depths of floodplain fine sediment above gravel and bedrock across the floodplain ranged from 0 to 141 cm with a mean value of 41 ± 25 cm (Table S2). A reach-based average migration rate of 0.24±0.05 m y^{-1} resulted in a mean migration distance of ~10.0±2.1 m along the probe transects for the entire period between 1973-2015 (Table S2). Error presented in the values above were propagated from the mean standard deviation of the estimated mean migration rates derived from the SCREAM analysis. Using our estimated vertical accretion rates at each point, we estimated an average vertical accretion rate of 3.3±0.3 cm y^{-1} among all points within the closest 10 m from the channel. The best performing multiple linear regression model explains ~60% of the variability in vertical accretion rates (r^2=0.60, p<0.001) using distance from the channel, relative elevation from the channel, valley confinement, local channel slope (all with p<0.001), and whether the survey point was on the inside of a bend (p=0.023; Table S4). A cell-by-cell multiple linear regression model of estimates of vertical accretion rates (r_{va}) across the floodplain (Figure S2) for each time period was developed based on distance from the channel (p< 0.001) and relative elevation from the channel (p<0.001). This model, readily parameterized from remotely-sensed data, explained ~54% of the variability in long-term vertical accretion rates over the 42-year time period between 1973 and 2015 (r^2=0.54, p<0.001) such that more deposition occurred closer to the channel and at lower elevations across the floodplain (Figure S2).

4.4 Eroded and Accreted Sediment Volumes

Estimated volumes of eroded and accreted sediment from the upper 2 km, intensive study reach were used to examine changes in volumes of floodplain sediment over the six time periods. Sediment input to and output from the floodplain during the six time periods ranged from 1145 ±258 to 17,324 ±2610 m^3 and 2713 ±113 to 11519 ±1851 m^3, respectively (Table 4). The difference between accreted and eroded volumes represent the net sediment change,

504 which ranged from -6273 ±2018 (where negative values indicate net erosion) to 10,683 ±3792
505 m^3 of sediment (Figure 2B, Table 4).

506 Estimated eroded volume exceeded accreted volume in all but one (i.e., 1955-1973) of
507 the six periods examined in this study resulting in a net loss of sediment over the total 60-year
508 time period between 1955 and 2015 (Figure 2B). Although the resulting estimated sediment
509 balance after 60 years was a net loss of 3919 m^3 across the floodplain during the 60-year
510 period, this net difference falls within the error of the estimate (i.e., ±5091 m^3) and suggest
511 closure of the sediment budget.

Table 4. Floodplain area and sediment volume eroded, accreted, and the net change between accretion and erosion along the upper 2 km, intensive study reach.

	1955 - 1973	1973 - 1983	1983 - 1990	1990 - 2001	2001 - 2011	2011 - 2015	Total
Duration (y)	18 ± 0.3	10 ± 0.3	7 ± 0.3	11 ± 0.3	10 ± 0.3	4 ± 0.3	
Area eroded (m^2)[a]	12228 ± 5060	12428 ± 2113	7341 ± 1835	16774 ± 2684	13317 ± 2530	3752 ± 1538	
Mean Depth of Eroded bank material (m)	0.54 ± 0.01	0.60 ± 0.01	0.58 ± 0.01	0.69 ± 0.01	0.61 ± 0.01	0.72 ± 0.01	
Volume Eroded (m^3)[b]	**-6640 ± 2751**	**-7476 ± 1277**	**-4272 ± 1071**	**-11519 ± 1851**	**-8080 ± 1541**	**-2713 ± 1113**	**-40700 ± 4169**
Mean erosion rate (m^3/y)	-369 ± 153	-748 ± 130	-610 ± 155	-1047 ± 171	-808 ± 156	-678 ± 283	
Mean bank area erosion rate (m^2/y)[c]	-0.02 ± 0.01	-0.04 ± 0.01	-0.03 ± 0.01	-0.06 ± 0.01	-0.04 ± 0.01	-0.04 ± 0.02	
Point bar area of accretion from (m^2)[d]	28392 ± 4356	12391 ± 1735	14534 ± 2035	13612 ± 2178	14493 ± 1884	7403 ± 1851	
Mean vertical accretion within eroded areas (m)[e]	0.59 ± 0.01	0.33 ± 0.01	0.23 ± 0.01	0.36 ± 0.01	0.33 ± 0.01	0.13 ± 0.01	
Estimated accretion along point bars (m^3)[f]	16865 ± 2608	4089 ± 587	3357 ± 493	4941 ± 803	4783 ± 640	977 ± 255	
Overbank deposition (m^3)[g]	459 ± 92	302 ± 61	213 ± 44	305 ± 62	322 ± 66	168 ± 36	
Total volume accreted (m^3)[h]	**17324 ± 2610**	**4391 ± 590**	**3570 ± 495**	**5246 ± 806**	**5105 ± 643**	**1145 ± 258**	**36780 ± 2921**
Mean accretion rate (m^3/y)	962.43 ± 145.87	439.11 ± 60.462	509.97 ± 73.961	476.9 ± 74.406	510.54 ± 66.126	286.16 ± 67.924	
Net volume (m^3)	**10684 ± 3792**	**-3085 ± 1407**	**-702 ± 1179**	**-6273 ± 2018**	**-2975 ± 1670**	**-1568 ± 1142**	**-3920 ± 5091**

[a] Area eroded from banks estimated by SCREAM (Rowland et al., 2016)
[b] Volume calculated directly in GIS
[c] Mean vertical area of bank eroded estimated as the mean erosion rate divided by the total channel length
[d] Area of point bar accretion estimated by SCREAM
[e] Vertical accretion estimated as the product of the duration of each time period and accretion rates derived from measured probe transect of fine floodplain sediment depths described in section 3.3
[f] Volume of accretion estimated as the product of accreted areas identified by SCREAM and mean vertical accretion rates
[g] Estimates of overbank deposition derived from the regression model described in section 3.4 in which vertical accretion rates of each DEM cell were summed and the total was multiplied by the number of years in each time period.
[h] The sum of accreted volumes from point bars and overbank deposition

4.5 Hydrologic linkages with floodplain sediment

Although each of the six time periods studied do not span equal time intervals, average flow conditions were similar for most time periods, with one drier and one wetter period (Figure 3C; Table 3). Peak discharge typically occurred within the second half of May, throughout June, and secondary peaks during high flow years sometimes occurred at the beginning of May and the beginning of July (Figure 3C; Table S3). The mean annual and peak discharges within the reach averaged 1.9 and 12.1 $m^3 s^{-1}$ respectively from 1935 to 2017. The period between 2012 and 2015 was a relatively dry interval with the least average number of days above both baseflow conditions and bankfull stage, the least mean and max annual volume of flow, the lowest maximum and mean peak flow, and the lowest mean and maximum total recession slope of all time periods (Table 3). Conversely, the period between 1991 and 2001 was a relatively wet interval with the highest mean duration above baseflow, the highest maximum peak flow, a relatively high total annual volume of discharge, and a relatively high number of peaks above bankfull flow conditions.

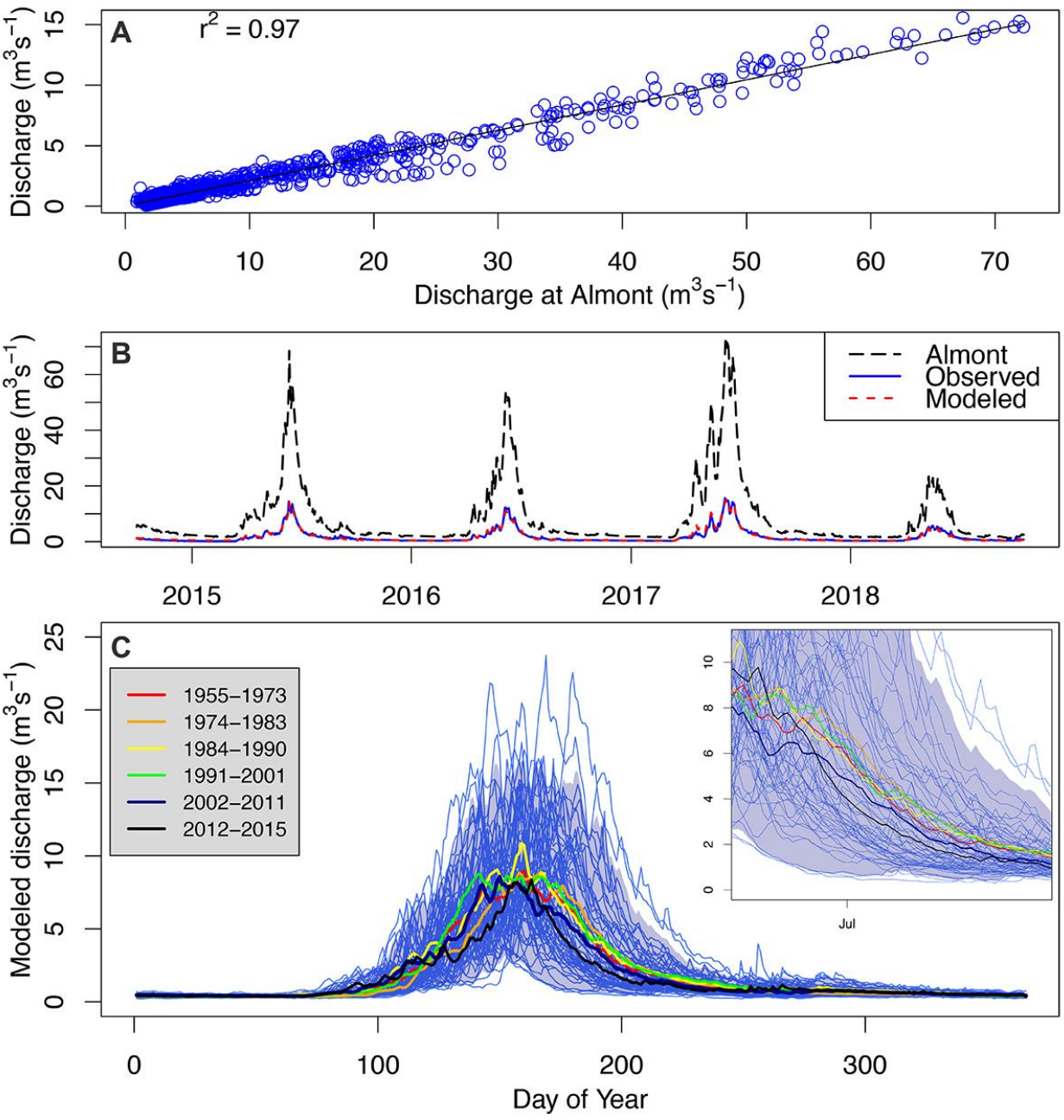

537

538 **Figure 3** Modeled discharge at the East River study site and Almont stream gauge. (A) Linear
539 regression between measured discharge at Almont and the study site (r^2=0.97), (B) discharge
540 at the two sites for the 2015 to 2018 water years including modeled discharge at the study site
541 based on the regression analysis (NSE=0.97). (C) Modeled annual hydrographs for the 60-year
542 study period (1955-2015) and an inset closeup of the hydrograph recession limbs. Thin, light
543 blue lines are annual hydrographs, the shaded blue area is the 95% confidence interval, and
544 colored lines represent mean hydrographs for the six time periods.

545

Multiple stepwise linear regression indicates that floodplain sediment exchange along the nine study reaches during the six time intervals are explained primarily by the hydrologic conditions and the sinuosity of the channel at the beginning of each period (Table S5). Laterally accreted area (A_L) with the appropriate power transformation (λ = 0.2626) was most significantly influenced by a positive correlation with sinuosity (*P; p <0.0001*), the maximum number of days above the reference baseflow condition (D_{base}*; p <0.05*), the mean channel width (w) of the study reach (p<0.05, and the maximum bankfull recession limb slope (R_{bf}) (r^2 = 0.55, p < 0.1).

$$A_L^{0.26263} = -6.591 + 0.015D_{base} + 3.142P + 0.240w + 21.432\ R_{bf} \quad (2)$$

The area of floodplain erosion (E_A) across the nine study reaches over the 6 periods was best explained by a positive correlation with the maximum total recession limb slope from peak to baseflow conditions (R_{total}*; p<0.0001*) and sinuosity (*P; p <0.001*) and a negative correlation with the maximum time between the first and last day flow exceeded baseflow (T_{base}) (r^2 = 0.59, p < 0.05; Table S5).

$$E_A^{0.10101} = 2.058 + 5.190\ R_{total} + 0.157\ P - 0.002\ T_{base} \quad (3)$$

Because our multiple linear regression analyses explained only about 55-60% of the variability in observed area of accretion and erosion and many variables examined require detailed analysis of imagery and lidar, we examined an additional simpler regression model using only the most significant variables that describe hydrologic conditions. Because sinuosity across the entire 11-km long study segment remains relatively constant and channel width similarly adjusts on a decadal time scale (Tables 1, 2), channel morphology maintains a quasi-steady state over the course of the study period. This means that changes in erosion and accretion may be explained by hydrology alone on a larger scale, under the primary assumptions of consistent sediment supply proportional to discharge. Such an approach is appealing because changes in hydrology are more easily measured by stream gauging, which allows predictions using future projections in climate variability.

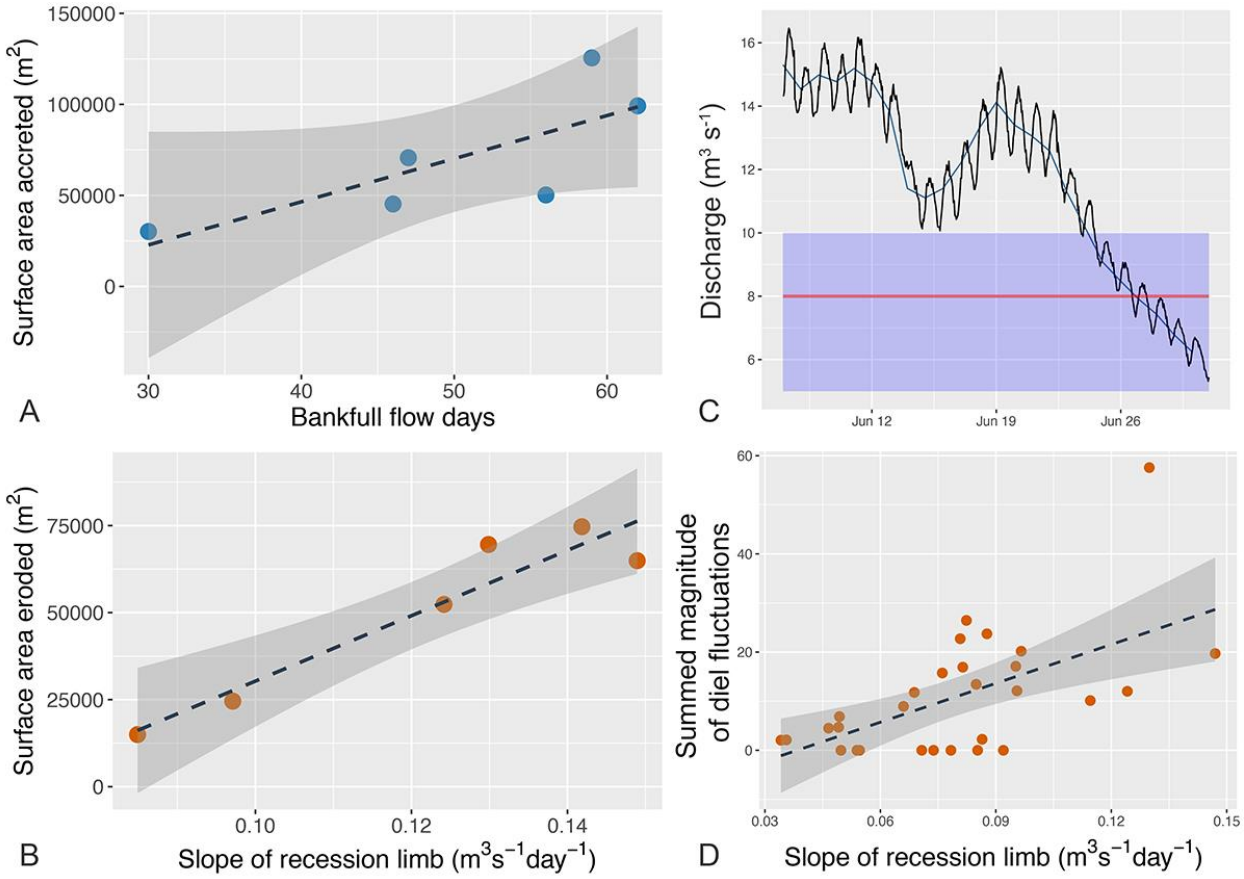

Figure 4 Linear regression of eroded and accreted areas and diel fluctuations. Each point represents each of the six time intervals for which data from all nine study reaches are combined. (A) The number of days that flow exceeded bankfull flow conditions is a significant predictor of accreted area (r^2=0.59, p = 0.074) and (B) the maximum slope within each time frame of the total recession limb from peak to baseflow is a significant predictor of eroded area (r^2=0.91, p = 0.003). (C) Fluctuations in discharge in response to snowmelt during daily warming and cooling cycles can exceed 3 m^3 s^{-1}, but do not show a strong correlation with the slope of the recession limb (r^2=0.29) (D). In A, B, and D, the dashed lines represent the linear regression model and the gray shaded area represents the 95% confidence intervals. In C the red line represents the bankfull flow stage and the blue shaded area represents the window in which diel fluctuations were examined.

Our analysis did not show a strong correlation between the maximum slope of the recession limb and number of, the summed magnitude, or the mean magnitude of diel fluctuations in discharge (Q = 8 m^3s^{-1}) within the defined bankfull window (5 < Q_{bf} < 12 m^3s^{-1}), but this topic requires more attention, particularly in snowmelt-dominated system that could change under a shifting climate.

589

590 Multiple linear regression to examine the role of hydrologic drivers alone on floodplain
591 sediment dynamics across the entire 11-km long study segment – in contrast to the regression
592 analyses that examined morphologic variables in addition to hydrologic variable across the nine
593 study reaches – identified similar variables as the most significant predictors of erosion and
594 accretion found in those other regression analyses. Examining hydrology alone, lateral accretion
595 across the entire 11-km long study segment was best explained by the maximum number of
596 days flow was above bankfull stage ($r^2 = 0.59$, $p = 0.074$; Figure 4A). The most significant
597 hydrologic variable for explaining the area of erosion along the 11-km long study segment was
598 the mean slope of the hydrograph recession from peak to baseflow conditions ($r^2 = 0.91$, $p =$
599 0.003; Figure 4B).

600 **4. Discussion**

601 4.1 Temporal variability of channel widening and narrowing

602 On the East River, we observed that progressive increases in sinuosity were truncated
603 by channel cutoffs. This autocylic pattern was punctuated with alternating periods of channel
604 narrowing and widening, which occur in tandem to maintain a relatively stable sinuosity on the
605 order of decades over the 11-km long study segment (Table 1; Figure 2A). The period between
606 2012 and 2015 is the only exception in this alternating pattern and may have arisen from a
607 reduction in erosion associated with the lowest maximum total recession slope in the study
608 period. Channel reaches are more likely to experience deposition and lateral accretion following
609 channel widening as flows spread out, flow depth decreases, and competency to transport
610 sediment declines. Germination of riparian species during high flows stabilize point bars,
611 resulting in channel narrowing that can force flow to outer banks and encourage subsequent
612 bank erosion (Merritt & Cooper, 2000; Zen et al., 2017). This type of feedback appears to have
613 occurred on the East River where narrowing induced increases in flow depth, velocity, and

614 boundary shear stress would have driven bank undercutting of the fine sediment facilitating
615 cantilever failure of saturated banks. Thus a window of opportunity for vegetation establishment
616 on bars (Balke et al., 2014; Caponi et al., 2019) followed by a substantial duration of overbank
617 flow that undercut banks would facilitate such a cyclical pattern. Propagation of cyclical patterns
618 of narrowing and widening have commonly been observed in the field (Hooke, 2008; Cantelli et
619 al., 2004) and modeled to match field observations after channel avulsions or bifurcations
620 (Kleinhans et al., 2011) like the chute cutoffs that occur on the East River.
621
622 4.2 Balancing the floodplain sediment budget and accretion
623 Of all the sources of possible error (i.e., lateral erosion and accretion, interpolation of
624 sediment volumes across the channel, and estimates of floodplain vertical accretion), vertical
625 accretion represents the most uncertain component of the sediment budget. Estimates of
626 deposition along point bars and areas adjacent to the channel are relatively robust because they
627 are based on measured long-term average deposition rates, but overbank deposition across the
628 entire floodplain based on our multiple linear regression contains uncertainty that cannot fully be
629 quantified. Our approach used a bulk depth of total sediment deposited over the 42 year period
630 between 1973 and 2015, which does not account for deposition and subsequent erosion
631 occurring at time scales shorter than our averaging.
632 Our regression analysis of lateral accretion does however examine hydrologic indices
633 that can incorporate the influences of annual events into the time period in which those events
634 occur (e.g., maximum bankfull volume, maximum cumulative days since last bankfull flow). The
635 duration between flow events has been referred to as the “window of opportunity” for riparian
636 vegetation to germinate and has been shown to be highly correlated with point bar accretion
637 (Balke et al., 2014; Zen et al., 2017; Caponi et al., 2019). Correlation were low between lateral
638 accretion and the maximum (r=0.232) and mean (r=-0.346) cumulative days since the last
639 bankfull flow and although the latter was higher, our results indicate a negative correlation

640 (Table S6). These variables were also eliminated for consideration in the optimal stepwise linear
641 regression model because of cross correlation (r = -0.79) with the most significant hydrologic
642 variable in the regression analysis, duration of overbank flow exceeding bankfull stage.
643 Our results linking (1) duration of overbank flows to lateral accretion and (2) distance
644 from the channel and relative elevation with overbank deposition support published research
645 that documents overbank deposition as a function of the duration of inundation and distance
646 from the channel (Asselman & Middelkoop, 1995; Hupp et al., 2008; G. Day et al., 2008).
647

648 4.3 *Linkages between hydrology and observed bank erosion*

649 Although the study presented here does not examine annual trends, our multiple
650 regression analysis results of nine study reaches and the simple relationship in Figure 4B
651 suggests that the slope of the peak annual recession limb is strongly linked to the occurrence of
652 bank erosion on the East River. While sinuosity and the maximum duration between the first
653 and last day of flow exceeding baseflow conditions are also significant predictors in the multiple
654 linear regression analysis ($p<0.01$), the recession limb slope has a higher significance
655 ($p<0.0001$). Although the volume of discharge above bankfull flow has been shown to be linked
656 to erosion (Surian, et al., 2015), this variable was eliminated from the analysis as a potential
657 predictor because of a strong correlation with the mean number of bankfull days ($r=0.98$). Other
658 variables eliminated from consideration as predictors for erosion because of high correlation
659 with the maximum total recession limb include variants of: the duration of baseflow, the bankfull
660 slope of the recession limb, and the cumulative number of days since the last bankfull flow.
661 The importance of the recession limb slope is emphasized by the fact that the maximum
662 total recession slope alone explains 91% of the variability in bank erosion when considering the
663 entire 11-km long study segment without separation into the nine study reaches. Past work by
664 Pizzuto (1994) in a snowmelt dominated system determined that elevated discharge for

665 approximately 7 days on the Powder River, Montana suggested a steep recession limb in 1978
666 may have been partially responsible for observed bank erosion on the order of 30% of the
667 channel width. Temporal resolution of aerial imagery does not provide the frequency needed to
668 examine past erosion on annual time scales on the East River. Hooke (1979) outlined a similar
669 challenge when examining the connection between bank erosion and hydrologic flow conditions
670 in temperate systems, because the study lacked the temporal resolution necessary to examine
671 the role of the recession limb in the observed rainfall-induced storm hydrograph peaks. The role
672 of the recession limb as a mechanism for bank erosion, however, likely varies substantially
673 between the temperate stormy system examined by Hooke and snowmelt-dominated discharge
674 of the East River.

675 Several mechanisms for river bank failures have been identified in prior research, as
676 described briefly in the introduction, but findings presented here that link flow conditions to
677 erosion may include a combination of mechanisms. On the East River, we observed that high
678 flows eroded underlying fluvial gravels resulting in planar cantilever failures of the fine grained
679 upper portion of the bank (Figure 1D, S1). Bank failures as a result of changes in river stage
680 may be triggered by a loss of confining pressure or slip failures resulting from positive pore
681 pressure, where slow drainage in saturated overlying banks of fine sediment cannot drain fast
682 enough to keep pace with the decline in stage (Rinaldi & Casagli, 1999). Positive pore pressure
683 is likely the case in stormy systems that experience flash floods with dramatic changes in
684 discharge occurring over the course of a single day or several hours, but could likely play a
685 partial role in bank erosion on the East River.

686 Shifting oblique directions in subsurface hydraulic gradient observed on the East River
687 (Malenda et al., 2019), could change the magnitude and direction of confining pressure on the
688 outside of river bends where erosion occurs and shifts hyporheic flow toward apposing meander
689 bends. This change in hydraulic gradient could produce a positive pore pressure along banks
690 with a seepage face, triggering bank erosion (Rinaldi & Casagli, 1999; Fox et al., 2007).

Although it is possible that some bank failures in the study area have been triggered by positive pore pressure, these types of failures often occur along much higher banks (>4m) composed of heterogeneous bank material, and slump scarps commonly provide evidence of occurrence (Simon et al., 2000; Langendoen & Simon, 2008; S. S. Day et al., 2013b). Slumps scarps are not observed on the East River, and cantilevers failures are the primary mechanism of bank failure.

Loss in confining pressure, provides a conceptual explanation for the link between observed cantilever failures and the slope of the recession limb in our analysis. Following undercutting during flows at or exceeding bankfull discharge, the gradual decline in flow stage occurring over the course of days to weeks and characteristic of snowmelt-dominated systems is likely to allow silt-dominated soils to drain so that undercut banks are no longer fully saturated (Figure 4). The loss of supporting pressure with declining stage can result in tension cracks of undercut banks that trigger bank failure (Rinaldi & Casagli, 1999). These cracks can be exacerbated by the weight of nearly saturated banks and repeat loss of supporting pressure from large diel fluctuations in discharge (2 to 5 m^3s^{-1}) during peak flow recessions on the East River near bankfull stage (~8 m^3s^{-1}; Figure 4C). These rapid changes in discharge (Q) equate to daily changes in flow depth (d) of approximately 20 to 30 cm at the gauging station which has an approximate bankfull width (w) of 14 m. Our analysis of diel fluctuations on an hourly time step from using USGS gage data from 1988 to 2018, however, does not show a strong correlation with the slope of the recession limb (Figure 4D), but this possible mechanism requires additional attention.

4.4 Influence of shifting hydrologic regimes on floodplain sediment fluxes

Observed increases in erosion linked to the total slope of the annual recession limb along the snowmelt-dominated East River in CO are likely to exist in other snowmelt-dominated systems that constitute a majority of rivers in the western USA (Li et al., 2017) and rivers above

717 40° latitude globally (Adam et al., 2009). Predicted increase in the frequency and severity of
718 storms and floods (Bates et al., 2008) could make extreme floods in mountainous regions – like
719 the one that occurred in the Colorado Front Range in 2013 – more common, which could greatly
720 alter floodplain sediment dynamics and residence times (Sutfin & Wohl, 2019). Observed
721 changes in snowpack (Stewart, 2009), upward shifts in the rainfall-snowfall transition (Kampf &
722 Lefsky, 2016), rapid warming and earlier snowmelt (Clow, 2009), increased rain-on-snow
723 events, are altering snow-melt dominated hydrographs (Stewart et al., 2004; Clow, 2009; Kampf
724 & Lefsky, 2016; Praskievicz, 2016; Painter et al., 2018). The coldest snowmelt regimes are
725 likely to experience increased spring hydrograph peaks, whereas transitional snowmelt regimes
726 may experience lower spring peaks and more winter peak events (Nijssen et al., 2001). Rain-
727 on-snow events in winter months could produce hydrograph peaks that exceed spring peaks in
728 snowmelt dominated systems. Although observations and projections of floods do not indicate
729 an increase in magnitude across rivers with all types of flow regimes, floods are occurring more
730 often (Hirsch & Archfield, 2015; Mallakpour & Villarini, 2015), which means more variability and
731 more frequent recession limbs in otherwise predictable and consistent snowmelt-dominated
732 systems. These changes would by definition shift otherwise predictable snowmelt dominated
733 systems to more flashy systems with increased variability and more rapidly rising and receding
734 limbs, but how changes could influence sediment dynamics are uncertain.

735 The changes in annual average snowpack and timing of snowmelt are poised to change
736 the variables identified in this study as important for both erosion and accretion, but the direction
737 of these changes in unknown. If a link between diel fluctuations and recession slope exists in
738 snowmelt-dominated systems stronger than that presented here, increased frequency of flood
739 peaks may not result in a substantial increase in bank erosion. However, if the link between the
740 recession slope and cantilever bank erosion occurs independently of diel fluctuations, increased
741 frequency and flashiness of flood peaks could equate to a significant increase in bank erosion
742 and alteration of floodplain sediment budgets. Because our results and other studies have

743 shown a positive correlation between floodplain accretion and the duration of overbank flow
744 (Asselman & Middelkoop, 1995; Hupp et al., 2008), flashier systems could limit overbank
745 deposition while encouraging bank erosion.
746
747 **Conclusion**
748 Analysis of aerial imagery, aerial lidar data, and field measurements of depth of
749 floodplain fine sediment suggest that the floodplain sediment budget along the East River study
750 segment is balanced over the 60-year study period. Empirical relationships between 60 years of
751 discharge data, channel morphometry of nine study reaches, and observed bank erosion and
752 accretion suggest that channel sinuosity is a significant factor for both erosion and accretion and
753 that channel width is a significant factor for the latter. In addition, the maximum slope of the
754 recession limb from the peak to baseflow and bankfull stage to baseflow as well as the duration
755 of flow above baseflow and bankfull conditions are significant hydrologic indices correlated with
756 erosion and accretion. The role of the hydrologic variables becomes more evident when
757 erosion and accretion are examined across the entire 11-km long study segment, rather than
758 the nine study reaches. Sixty percent of the variability in accretion is explained by the maximum
759 number of flow days exceeding bankfull stage and 91% of erosion is explained by the maximum
760 slope of the annual peak recession limb within each time period. We posit that diel fluctuations
761 during the annual recession on the order of 25% of the bankfull flow play a role in observed
762 cantilever failures, but our analysis does not show a strong relationship between recession
763 slope and diel fluctuations. Projected changes and increased variability in flow regimes of
764 snowmelt-dominated systems are likely to influence the variables identified here as important for
765 floodplain sediment dynamics in other regions.
766
767 **Acknowledgement:**

This work was funded by an Early Career award to Rowland by the Subsurface Biogeochemical Research Programs within the U.S. Department of Energy Office of Science, Biological and Environmental Research Program. This material is partially based upon work supported through the Lawrence Berkeley National Laboratory's Watershed Function Scientific Focus Area (operated by the University of California) funded by the U.S. Department of Energy (DOE), Office of Science, Office of Biological and Environmental Research contract DE-AC02-05CH11231. We thank the Rocky Mountain Biological Research Station for their support and Meghan King and Anastasia Piliouras for their assistance in the field. All data used for this study are provided in the manuscript, as supplemental materials, and in Sutfin & Rowland (2019) and Carroll & Williams (2019). The R code used to extract hydrologic parameters are provided as supplemental Supporting Information as cited in the text. This manuscript was greatly improved by comments from two anonymous reviewers and the associate editor.

References

Adam, J. C., Hamlet, A. F., & Lettenmaier, D. P. (2009). Implications of global climate change for snowmelt hydrology in the twenty-first century. *Hydrological Processes*, *23*(7), 962–972. https://doi.org/10.1002/hyp.7201

Asselman, N. E. M., & Middelkoop, H. (1995). Floodplain sedimentation: Quantities, patterns and processes. *Earth Surface Processes and Landforms*, *20*(6), 481–499. https://doi.org/10.1002/esp.3290200602

Balke, T., Herman, P. M. J., & Bouma, T. J. (2014). Critical transitions in disturbance-driven ecosystems: identifying Windows of Opportunity for recovery. *Journal of Ecology*, *102*(3), 700–708. https://doi.org/10.1111/1365-2745.12241

Bates, B., Kundzewicz, Z. W., Wu, S., Burkett, V., Doell, P., Gwary, D., et al. (2008). *Climate Change and Water. Technical Paper of the Intergovernmental Panel on Climate Change*.

Belmont, P., Gran, K. B., Schottler, S. P., Wilcock, P. R., Day, S. S., Jennings, C., et al. (2011). Large Shift in Source of Fine Sediment in the Upper Mississippi River. *Environmental Science & Technology*, *45*(20), 8804–8810. https://doi.org/10.1021/es2019109

Benjankar, R., Burke, M., Yager, E., Tonina, D., Egger, G., Rood, S. B., & Merz, N. (2014). Development of a spatially-distributed hydroecological model to simulate cottonwood seedling recruitment along rivers. *Journal of Environmental Management*, *145*, 277–288. https://doi.org/10.1016/j.jenvman.2014.06.027

Bogoni, M., Putti, M., & Lanzoni, S. (2017). Modeling meander morphodynamics over self-formed heterogeneous floodplains. *Water Resources Research*, *53*(6), 5137–5157. https://doi.org/10.1002/2017WR020726

Cantelli, A., Paola, C., & Parker, G. (2004). Experiments on upstream-migrating erosional narrowing and widening of an incisional channel caused by dam removal. *Water Resources Research*, *40*(3). https://doi.org/10.1029/2003WR002940

Caponi, F., Koch, A., Bertoldi, W., Vetsch, D. F., & Siviglia, A. (2019). When Does Vegetation Establish on Gravel Bars? Observations and Modeling in the Alpine Rhine River. *Frontiers in Environmental Science*, *7*. https://doi.org/10.3389/fenvs.2019.00124

Carroll, R., & Williams, K. (2019). Discharge data collected within the East River for the Lawrence Berkeley National Laboratory Watershed Function Science Focus Area (water years 2015-2018), Watershed Function SFA. *EES-DIVE: Deep Insight for Earth Science*. http://dx.doi.org/10.21952/WTR/1495380

Clow, D. W. (2009). Changes in the Timing of Snowmelt and Streamflow in Colorado: A Response to Recent Warming. *Journal of Climate*, *23*(9), 2293–2306. https://doi.org/10.1175/2009JCLI2951.1

816 Darby, S. E., Rinaldi, M., & Dapporto, S. (2007). Coupled simulations of fluvial erosion and
817 mass wasting for cohesive river banks. *Journal of Geophysical Research: Earth Surface,*
818 *112*(F3). https://doi.org/10.1029/2006JF000722
819 Day, G., Dietrich, W. E., Rowland, J. C., & Marshall, A. (2008). The depositional web on the
820 floodplain of the Fly River, Papua New Guinea. *Journal of Geophysical Research: Earth*
821 *Surface, 113*. https://doi.org/10.1029/2006JF000622@10.1002/(ISSN)2169-
822 9011.PAPUA1
823 Day, S. S., Gran, K. B., Belmont, P., & Wawrzyniec, T. (2013a). Measuring bluff erosion part 1:
824 terrestrial laser scanning methods for change detection. *Earth Surface Processes and*
825 *Landforms, 38*(10), 1055–1067. https://doi.org/10.1002/esp.3353
826 Day, S. S., Gran, K. B., Belmont, P., & Wawrzyniec, T. (2013b). Measuring bluff erosion part 2:
827 pairing aerial photographs and terrestrial laser scanning to create a watershed scale
828 sediment budget. *Earth Surface Processes and Landforms, 38*(10), 1068–1082.
829 https://doi.org/10.1002/esp.3359
830 Dietrich, W. E., Dunne, T., Humphrey, N. F., & Reid, L. M. (1982). Construction of sediment
831 budgets for drainage basins. *In: Sediment Budgets and Routing in Forested Drainage*
832 *Basins: Proceedings of the Symposium; 31 May - 1 June 1982; Corvallis, Oregon. Gen.*
833 *Tech. Rep. PNW-141. Portland, Oregon: Pacific Northwest Forest and Range*
834 *Experiment Station, Forest Service, U.S. Department of Agriculture; 1982: 5-23.*
835 Retrieved from https://www.fs.usda.gov/treesearch/pubs/7749
836 Donovan, M., Belmont, P., Notebaert, B., Coombs, T., Larson, P., & Souffront, M. (2019).
837 Accounting for uncertainty in remotely-sensed measurements of river planform change.
838 *Earth-Science Reviews, 193*, 220–236. https://doi.org/10.1016/j.earscirev.2019.04.009

Dormann, C. F., Elith, J., Bacher, S., Buchmann, C., Carl, G., Carré, G., et al. (2013). Collinearity: a review of methods to deal with it and a simulation study evaluating their performance. *Ecography*, *36*(1), 27–46. https://doi.org/10.1111/j.1600-0587.2012.07348.x

Fisher, G. B., Bookhagen, B., & Amos, C. B. (2013). Channel planform geometry and slopes from freely available high-spatial resolution imagery and DEM fusion: Implications for channel width scalings, erosion proxies, and fluvial signatures in tectonically active landscapes. *Geomorphology*, *194*, 46–56. https://doi.org/10.1016/j.geomorph.2013.04.011

Fox, G. A., Wilson, G. V., Simon, A., Langendoen, E. J., Akay, O., & Fuchs, J. W. (2007). Measuring streambank erosion due to ground water seepage: correlation to bank pore water pressure, precipitation and stream stage. *Earth Surface Processes and Landforms*, *32*(10), 1558–1573. https://doi.org/10.1002/esp.1490

Gaskill, D. L., Mutschler, F. E., Kramer, J. H., Thomas, J. A., & Zahony, S. G. (1991). Geologic map of the Gothic quadrangle, Gunnison County, Colorado. Geologic Quadrangle Map GQ-1689, sale 1:24,000, Gunnison, Colorado: U.S. Geological Survey.

Gellis, A. C., & Walling, D. E. (2013). Sediment Source Fingerprinting (Tracing) and Sediment Budgets as Tools in Targeting River and Watershed Restoration Programs. In A. Simon, S. J. Bennett, & J. M. Castro (Eds.), *Geophysical Monograph Series* (pp. 263–291). Washington, D. C.: American Geophysical Union. https://doi.org/10.1029/2010GM000960

Gellis, A. C., Pavich, M. J., Ellwein, A. L., Aby, S., Clark, I., Wieczorek, M. E., & Viger, R. (2012). Erosion, storage, and transport of sediment in two subbasins of the Rio Puerco, New Mexico. *GSA Bulletin*, *124*(5–6), 817–841. https://doi.org/10.1130/B30392.1

Güneralp, İ., & Rhoads, B. L. (2009). Empirical analysis of the planform curvature-migration relation of meandering rivers. *Water Resources Research*, *45*(9), W09424. https://doi.org/10.1029/2008WR007533

Gurnell, A. M. (1997). Channel change on the River Dee meanders, 1946–1992, from the analysis of air photographs. *Regulated Rivers: Research & Management*, *13*(1), 13–26. https://doi.org/10.1002/(SICI)1099-1646(199701)13:1<13::AID-RRR420>3.0.CO;2-W

Hirsch, R. M., & Archfield, S. A. (2015). Flood trends: Not higher but more often. *Nature Climate Change*, *5*(3), 198–199. https://doi.org/10.1038/nclimate2551

Hoffmann, T., Glatzel, S., & Dikau, R. (2009). A carbon storage perspective on alluvial sediment storage in the Rhine catchment. *Geomorphology*, *108*(1), 127–137. https://doi.org/10.1016/j.geomorph.2007.11.015

Hooke, J. M. (1979). An analysis of the processes of river bank erosion. *Journal of Hydrology*, *42*(1), 39–62. https://doi.org/10.1016/0022-1694(79)90005-2

Hooke, J. M. (2008). Temporal variations in fluvial processes on an active meandering river over a 20-year period. *Geomorphology*, *100*(1), 3–13. https://doi.org/10.1016/j.geomorph.2007.04.034

Howard, A. D. (1996). Modeling Channel Evolution and Floodplain Morphology. *Floodplain Processes*, 15–62.

Hupp, C. R., Demas, C. R., Kroes, D. E., Day, R. H., & Doyle, T. W. (2008). Recent sedimentation patterns within the central Atchafalaya Basin, Louisiana. *Wetlands*, *28*(1), 125–140. https://doi.org/10.1672/06-132.1

Kampf, S. K., & Lefsky, M. A. (2016). Transition of dominant peak flow source from snowmelt to rainfall along the Colorado Front Range: Historical patterns, trends, and lessons from the 2013 Colorado Front Range floods. *Water Resources Research*, *52*(1), 407–422. https://doi.org/10.1002/2015WR017784

Kleinhans, M. G., Cohen, K. M., Hoekstra, J., & IJmker, J. M. (2011). Evolution of a bifurcation in a meandering river with adjustable channel widths, Rhine delta apex, The Netherlands. *Earth Surface Processes and Landforms*, *36*(15), 2011–2027. https://doi.org/10.1002/esp.2222

Langendoen, E. J., & Alonso, C. V. (2008). Modeling the Evolution of Incised Streams: I. Model Formulation and Validation of Flow and Streambed Evolution Components. *Journal of Hydraulic Engineering*, *134*(6), 749–762. https://doi.org/10.1061/(ASCE)0733-9429(2008)134:6(749)

Langendoen, E. J., & Simon, A. (2008). Modeling the Evolution of Incised Streams. II: Streambank Erosion. *Journal of Hydraulic Engineering*, *134*(7), 905–915. https://doi.org/10.1061/(ASCE)0733-9429(2008)134:7(905)

Lenhart, C. F., Titov, M. L., Ulrich, J. S., Nieber, J. L., & Suppes, B. J. (2013). The Role of Hydrologic Alteration and Riparian Vegetation Dynamics in Channel Evolution along the Lower Minnesota River. *Transactions of the American Society of Agricultural and Biological Engineers*, *56*(2), 549–561.

Li, D., Wrzesien, M. L., Durand, M., Adam, J., & Lettenmaier, D. P. (2017). How much runoff originates as snow in the western United States, and how will that change in the future? *Geophysical Research Letters*, *44*(12), 6163–6172. https://doi.org/10.1002/2017GL073551

Lininger, K. B., Wohl, E., Rose, J. R., & Leisz, S. J. (2019). Significant Floodplain Soil Organic Carbon Storage Along a Large High-Latitude River and its Tributaries. *Geophysical Research Letters*, *46*(4), 2121–2129. https://doi.org/10.1029/2018GL080996

Macklin, M. G., Brewer, P. A., Hudson-Edwards, K. A., Bird, G., Coulthard, T. J., Dennis, I. A., et al. (2006). A geomorphological approach to the management of rivers contaminated by metal mining. *Geomorphology*, *79*(3), 423–447. https://doi.org/10.1016/j.geomorph.2006.06.024

Malenda, H. f., Sutfin, N. a., Guryan, G., Stauffer, S., Rowland, J. c., Williams, K. h., & Singha, K. (2019). From Grain to Floodplain: Evaluating heterogeneity of floodplain hydrostatigraphy using sedimentology, geophysics, and remote sensing. *Earth Surface Processes and Landforms*, *0*(0). https://doi.org/10.1002/esp.4613

Mallakpour, I., & Villarini, G. (2015). The changing nature of flooding across the central United States. *Nature Climate Change*, *5*(3), 250–254. https://doi.org/10.1038/nclimate2516

McFeeters, S. K. (1996). The use of the Normalized Difference Water Index (NDWI) in the delineation of open water features. *International Journal of Remote Sensing*, *17*(7), 1425–1432. https://doi.org/10.1080/01431169608948714

Merritt, D. M., & Cooper, D. J. (2000). Riparian vegetation and channel change in response to river regulation: a comparative study of regulated and unregulated streams in the Green

River Basin, USA. *Regulated Rivers: Research & Management*, *16*(6), 543–564. https://doi.org/10.1002/1099-1646(200011/12)16:6<543::AID-RRR590>3.0.CO;2-N

Micheli, E. R., & Kirchner, J. W. (2002a). Effects of wet meadow riparian vegetation on streambank erosion. 1. Remote sensing measurements of streambank migration and erodibility. *Earth Surface Processes and Landforms*, *27*(6), 627–639. https://doi.org/10.1002/esp.338

Micheli, E. R., & Kirchner, J. W. (2002b). Effects of wet meadow riparian vegetation on streambank erosion. 2. Measurements of vegetated bank strength and consequences for failure mechanics. *Earth Surface Processes and Landforms*, *27*(7), 687–697. https://doi.org/10.1002/esp.340

Mount, N., & Louis, J. (2005). Estimation and propagation of error in measurements of river channel movement from aerial imagery. *Earth Surface Processes and Landforms*, *30*(5), 635–643. https://doi.org/10.1002/esp.1172

Naiman, R. J., Decamps, H., & McClain, M. E. (2010). *Riparia: Ecology, Conservation, and Management of Streamside Communities*. Elsevier.

Nijssen, B., O'Donnell, G. M., Hamlet, A. F., & Lettenmaier, D. P. (2001). Hydrologic Sensitivity of Global Rivers to Climate Change. *Climatic Change*, *50*(1), 143–175. https://doi.org/10.1023/A:1010616428763

Noe, G. B., & Hupp, C. R. (2005). Carbon, nitrogen, and phosphorus accumulation in floodplains of atlantic coastal plain rivers, usa. *Ecological Applications*, *15*(4), 1178–1190. https://doi.org/10.1890/04-1677

Omengo, F. O., Geeraert, N., Bouillon, S., & Govers, G. (2018). Deposition and fate of organic carbon in floodplains along a tropical semiarid lowland river (Tana River, Kenya).

Journal of Geophysical Research: Biogeosciences, 1131–1143. https://doi.org/10.1002/2015JG003288@10.1002/(ISSN)2169-8961.CNFLOI1

Painter, T. H., Skiles, S. M., Deems, J. S., Brandt, W. T., & Dozier, J. (2018). Variation in Rising Limb of Colorado River Snowmelt Runoff Hydrograph Controlled by Dust Radiative Forcing in Snow. *Geophysical Research Letters*, *45*(2), 797–808. https://doi.org/10.1002/2017GL075826

Parker, G., Shimizu, Y., Wilkerson, G. V., Eke, E. C., Abad, J. D., Lauer, J. W., et al. (2011). A new framework for modeling the migration of meandering rivers. *Earth Surface Processes and Landforms*, *36*(1), 70–86. https://doi.org/10.1002/esp.2113

Parker, Gary, Sawai, K., & Ikeda, S. (1982). Bend theory of river meanders. Part 2. Nonlinear deformation of finite-amplitude bends. *Journal of Fluid Mechanics*, *115*, 303–314. https://doi.org/10.1017/S0022112082000767

Pizzuto, J. E., & Meckelnburg, T. S. (1989). Evaluation of a linear bank erosion equation. *Water Resources Research*, *25*(5), 1005–1013. https://doi.org/10.1029/WR025i005p01005

Pizzuto, James E. (1994). Channel adjustments to changing discharges, Powder River, Montana. *GSA Bulletin*, *106*(11), 1494–1501. https://doi.org/10.1130/0016-7606(1994)106<1494:CATCDP>2.3.CO;2

Poff, N. L., Allan, J. D., Bain, M. B., Karr, J. R., Prestegaard, K. L., Richter, B. D., et al. (1997). The Natural Flow Regime. *BioScience*, *47*(11), 769–784. https://doi.org/10.2307/1313099

Praskievicz, S. (2016). Impacts of Projected Climate Changes on Streamflow and Sediment Transport for Three Snowmelt-Dominated Rivers in the Interior Pacific Northwest. *River Research and Applications*, *32*(1), 4–17. https://doi.org/10.1002/rra.2841

Reid, L., & Dunne, T. (2016). Sediment budgets as an organizing framework in fluvial geomorphology. *In: Kondolf, G.M.; Piégay, H., Eds. Tools in Fluvial Geomorphology. Chichester, UK: John Wiley & Sons, Ltd: 357-379. Chapter 16*, 357–379. https://doi.org/10.1002/9781118648551

Rhoades, E. L., O'Neal, M. A., & Pizzuto, J. E. (2009). Quantifying bank erosion on the South River from 1937 to 2005, and its importance in assessing Hg contamination. *Applied Geography*, *29*(1), 125–134. https://doi.org/10.1016/j.apgeog.2008.08.005

Richard, G. A., Julien, P. Y., & Baird, D. C. (2005). Statistical analysis of lateral migration of the Rio Grande, New Mexico. *Geomorphology*, *71*(1), 139–155. https://doi.org/10.1016/j.geomorph.2004.07.013

Richter, B. D., Baumgartner, J. V., Powell, J., & Braun, D. P. (1996). A Method for Assessing Hydrologic Alteration within Ecosystems. *Conservation Biology*, *10*(4), 1163–1174. https://doi.org/10.1046/j.1523-1739.1996.10041163.x

Rinaldi, M., & Casagli, N. (1999). Stability of streambanks formed in partially saturated soils and effects of negative pore water pressures: the Sieve River (Italy). *Geomorphology*, *26*(4), 253–277. https://doi.org/10.1016/S0169-555X(98)00069-5

Rodriguez-Freire, L., Avasarala, S., Ali, A.-M. S., Agnew, D., Hoover, J. H., Artyushkova, K., et al. (2016). Post Gold King Mine Spill Investigation of Metal Stability in Water and Sediments of the Animas River Watershed. *Environmental Science & Technology*, *50*(21), 11539–11548. https://doi.org/10.1021/acs.est.6b03092

Rowland, J. C., Shelef, E., Pope, P. A., Muss, J., Gangodagamage, C., Brumby, S. P., & Wilson, C. J. (2016). A morphology independent methodology for quantifying planview river

change and characteristics from remotely sensed imagery. *Remote Sensing of Environment*, *184*, 212–228. https://doi.org/10.1016/j.rse.2016.07.005

Schook, D. M., Rathburn, S. L., Friedman, J. M., & Wolf, J. M. (2017). A 184-year record of river meander migration from tree rings, aerial imagery, and cross sections. *Geomorphology*, *293*, 227–239. https://doi.org/10.1016/j.geomorph.2017.06.001

Schwenk, J., Khandelwal, A., Fratkin, M., Kumar, V., & Foufoula-Georgiou, E. (2017). High spatiotemporal resolution of river planform dynamics from Landsat: The RivMAP toolbox and results from the Ucayali River. *Earth and Space Science*, *4*(2), 2016EA000196. https://doi.org/10.1002/2016EA000196

Scott, D. N., & Wohl, E. E. (2018). Geomorphic regulation of floodplain soil organic carbon concentration in watersheds of the Rocky and Cascade Mountains, USA. *Earth Surface Dynamics*, *6*(4), 1101–1114. https://doi.org/10.5194/esurf-6-1101-2018

Sekely, A. C., Mulla, D. J., & Bauer, D. W. (2002). Streambank slumping and its contribution to the phosphorus and suspended sediment loads of the blue earth river, minnesota. *Journal of Soil and Water Conservation*, *57*(5), 243–250.

Simon, A., Curini, A., Darby, S. E., & Langendoen, E. J. (2000). Bank and near-bank processes in an incised channel. *Geomorphology*, *35*(3), 193–217. https://doi.org/10.1016/S0169-555X(00)00036-2

Simon, A., Thomas, R. E., Curini, A., & Shields, F. D. (2002). Case Study: Channel Stability of the Missouri River, Eastern Montana. *Journal of Hydraulic Engineering*, *128*(10), 880–890. https://doi.org/10.1061/(ASCE)0733-9429(2002)128:10(880)

Stewart, I. T. (2009). Changes in snowpack and snowmelt runoff for key mountain regions. *Hydrological Processes*, *23*(1), 78–94. https://doi.org/10.1002/hyp.7128

Stewart, I. T., Cayan, D. R., & Dettinger, M. D. (2004). Changes in Snowmelt Runoff Timing in Western North America under a `Business as Usual' Climate Change Scenario. *Climatic Change*, *62*(1), 217–232. https://doi.org/10.1023/B:CLIM.0000013702.22656.e8

Sutfin, N. A., & Rowland, J. C. (2019). Depth and elevation of floodplain fine sediment along the East River near Crested Butte, Colorado measured in 2016 and 2017. Incorporating the Hydrological Controls on Carbon Cycling in Floodplain Ecosystems into Earth System Models (ESMs). *ESS-Dive: Deep Insight for Earth Science Data*. https://doi.org/doi:10.15485/1574502

Sutfin, N. A., & Wohl, E. (2017). Substantial soil organic carbon retention along floodplains of mountain streams. *Journal of Geophysical Research: Earth Surface*, *122*(7), 1325–1338. https://doi.org/10.1002/2016JF004004

Sutfin, N. A., & Wohl, E. (2019). Elevational differences in hydrogeomorphic disturbance regime influence sediment residence times within mountain river corridors. *Nature Communications*, *10*(1), 2221. https://doi.org/10.1038/s41467-019-09864-w

Sutfin, N. A., Wohl, E. E., & Dwire, K. A. (2016). Banking carbon: a review of organic carbon storage and physical factors influencing retention in floodplains and riparian ecosystems. *Earth Surface Processes and Landforms*, *41*(1), 38–60. https://doi.org/10.1002/esp.3857

Surian, N., Barban, M., Ziliani, L., Monegato, G., Bertoldi, W., & Comiti, F. (2015). Vegetation turnover in a braided river: frequency and effectiveness of floods of different magnitude. *Earth Surface Processes and Landforms*, *40*(4), 542–558. https://doi.org/10.1002/esp.3660

Theobald, D. M., Gosnell, H., & Riebsame, W. E. (1996). Land Use and Landscape Change in the Colorado Mountains II: A Case Study of the East River Valley. *Mountain Research and Development*, *16*(4), 407–418. https://doi.org/10.2307/3673990

Thorne, C. R., & Tovey, N. K. (1981). Stability of composite river banks. *Earth Surface Processes and Landforms*, *6*(5), 469–484. https://doi.org/10.1002/esp.3290060507

Wohl, E., Dwire, K., Sutfin, N., Polvi, L., & Bazan, R. (2012). Mechanisms of carbon storage in mountainous headwater rivers. *Nature Communications*, *3*, 1263. https://doi.org/10.1038/ncomms2274

Wohl, E., Bledsoe, B. P., Jacobson, R. B., Poff, N. L., Rathburn, S. L., Walters, D. M., & Wilcox, A. C. (2015). The Natural Sediment Regime in Rivers: Broadening the Foundation for Ecosystem Management. *BioScience*, *65*(4), 358–371. https://doi.org/10.1093/biosci/biv002

Wolman, M. G. (1959). Factors Influencing Erosion of a Cohesive River Bank. *American Journal of Science*, *257*(3), 204–216. https://doi.org/10.2475/ajs.257.3.204

Zen, S., Gurnell, A. M., Zolezzi, G., & Surian, N. (2017). Exploring the role of trees in the evolution of meander bends: The Tagliamento River, Italy. *Water Resources Research*, *53*(7), 5943–5962. https://doi.org/10.1002/2017WR020561

Year	Floodplain area (km2)	Channel Area (km2)	Channel Length (km)	Sinuosity (m/m)	Channel slope (%)
1955	2193.6	459.0	20.08	1.89	0.339%
1973	2254.0	398.7	19.29	1.82	0.353%
1983	2222.3	430.3	18.80	1.77	0.362%
1990	2295.4	357.3	18.90	1.78	0.361%
2001	2275.4	377.3	19.39	1.83	0.352%
2011	2296.2	356.5	18.81	1.77	0.362%
2015	2312.2	340.4	18.98	1.79	0.359%

Confinement (m2/m2)	Mean channel width (m)
0.17	25 ± 2
0.15	20 ± 2
0.16	23 ± 3
0.13	19 ± 3
0.14	21 ± 3
0.13	19 ± 1
0.13	17 ± 1

Reach	Valley area (m^2)	Valley Length (m)	Valley slope (%)	Floodplain area (m^2)	Channel Area (m2)
1	344236	1471	0.94	294462	49774 ± 6292
2	489119	2126	0.74	405784	83334 ± 6234
3	232658	910	0.55	199873	32785 ± 6046
4	93445	595	0.86	76134	17311 ± 1495
5	330488	1142	0.68	283494	46994 ± 5334
6	378666	924	0.56	344169	34497 ±4194
7	302210	855	0.33	271371	30839 ± 6166
8	126101	1175	0.54	89108	36992 ± 2469
9	355743	1420	0.46	299779	55965 ± 8114

Channel Length (m)	Sinuosity (m/m)	Channel slope (%)	Confinement (m^2/m^2)	Channel
2860 ± 130	1.94 ± 0.09	0.48 ± 0.02	0.14 ± 0.02	18
4735 ± 143	2.23 ± 0.07	0.33 ± 0.01	0.17 ± 0.01	18
1740 ± 99	1.91 ± 0.11	0.29 ± 0.02	0.14 ± 0.03	19
903 ± 60	1.52 ± 0.10	0.57 ± 0.04	0.19 ± 0.02	20
2419 ± 170	2.12 ± 0.15	0.32 ± 0.02	0.14 ± 0.02	20
1448 ± 248	1.57 ± 0.27	0.37 ± 0.06	0.09 ± 0.01	22
1490 ± 116	1.74 ± 0.14	0.19 ± 0.02	0.1 ± 0.02	21
1583 ± 26	1.35 ± 0.02	0.4 ± 0.01	0.29 ± 0.02	23
2001 ± 53	1.41 ± 0.04	0.33 ± 0.01	0.16 ± 0.02	23

width (m)
± 3
± 2
± 3
± 2
± 2
± 3
± 3
± 3
± 4

	1955-1973	1973-1983	1983-1990	1990-2001	2001-2011	2011-2015	Mean	Total
Duration (years)	18 ± 0.3	10 ± 0.3	7 ± 0.3	11 ± 0.3	10 ± 0.3	4 ± 0.3	10 ± 0.3	60 ± 0.8
Accretion (m^2)	125529 ± 27774	45276 ± 6339	99194 ± 13887	50226 ± 8036	70686 ± 9189	30156 ± 7539	70178 ± 12127	421067 ± 34789
Erosion (m^2)	-64915 ± 25388	-74670 ± 12694	-24569 ± 6142	-69550 ± 11128	-52358 ± 9948	-14969 ± 6137	-50172 ± 11906	-301031 ± 33224
Net Change (m^2)	60614 ± 37629	-29394 ± 14188	74625 ± 15185	-19324 ± 13726	18328 ± 13543	15187 ± 9721	20006 ± 17332	120036 ± 48106
Accretion Rate ($m^2 y^{-1}$)	6974 ± 1548	4528 ± 652	14171 ± 2095	4566 ± 744	7069 ± 949	7539 ± 1987	7474 ± 1329	44846 ± 3551
Erosion Rate ($m^2 y^{-1}$)	-3606 ± 1412	-7467 ± 1294	-3510 ± 893	-6323 ± 1030	-5236 ± 1010	-3742 ± 1566	-4981 ± 1201	-29884 ± 2999
Mean linear Accretion Rate ($m\ y^{-1}$)	0.347 ± 0.077	0.235 ± 0.034	0.754 ± 0.111	0.242 ± 0.039	0.365 ± 0.049	0.401 ± 0.106	0.390 ± 0.069	2.343 ± 0.186
Mean Linear Erosion Rate ($m\ y^{-1}$)	-0.180 ± 0.070	-0.387 ± 0.067	-0.187 ± 0.048	-0.334 ± 0.054	-0.270 ± 0.052	-0.199 ± 0.083	-0.259 ± 0.062	-1.557 ± 0.156
Mean Day of Peak Flow	152.7	162	156.3	151.5	147	155.3	154.13 ± 5.06	
Mean Peak Flow ($m^3 s^{-1}$)	11.84	11.6	12.9	12.35	11.31	10.15	11.69 ± 0.94	
Max Peak Flow ($m^3 s^{-1}$)	22.56	18.32	21.86	23.74	16.02	15.49	19.67 ± 3.53	
Mean Bankfull Duration (days)	31.3	38.1	41	36.1	29.3	25.5	33.55 ± 5.84	
Max Bankfull Duration (days)	61	48	64	63	47	31	52.33 ± 12.86	
Mean Days Above Bankfull Flow	20.3	24	22.6	23.8	18.5	12.8	20.33 ± 4.26	
Max Days Above Bankfull Flow	59	46	62	56	47	30	50.00 ± 11.71	
Mean Duration Above Baseflow (days)	215.5	218	255.1	230.9	263	278.5	243.50 ± 25.82	
Max Duration Above Baseflow (days)	362	331	364	305	364	349	345.83 ± 23.74	
Mean Days Above Baseflow	232.1	217.8	266.7	243.9	259.8	245.5	244.30 ± 17.86	
Max Days Above Baseflow	281	261	362	275	316	272	294.50 ± 37.97	
Mean Days Since Bankfull Flow	267	327.1	349.6	261.3	345.3	455.3	334.27 ± 70.58	
Max Days Since Bankfull Flow	925	904	935	579	944	901	864.67 ± 140.96	
Mean Day Baseflow Ends	280.2	288.6	304	305.3	291	321.3	298.40 ± 14.73	
Mean Day Bankfull Flow Ends	173.3	181.9	176.8	172.7	170.3	173	174.67 ± 4.11	
Mean No. Peaks Above Bankfull		1.9	2	1.8	1.4	0.5	1.52 ± 0.61	
Maximum No. Peaks Above Bankfull	3	4	5	4	3	1	3.33 ± 1.37	
Mean Total Recession Slope ($m^3 s^{-1} day^{-1}$)	0.094	0.087	0.083	0.077	0.079	0.056	0.08 ± 0.01	
Max Total Recession Slope ($m^3 s^{-1} day^{-1}$)	0.149	0.142	0.097	0.13	0.124	0.085	0.12 ± 0.03	
Mean Bankfull Recession Slope ($m^3 s^{-1} day^{-1}$)	0.076	0.064	0.059	0.058	0.066	0.047	0.06 ± 0.01	
Max Bankfull Recession Slope ($m^3 s^{-1} day^{-1}$)	0.12	0.086	0.082	0.075	0.091	0.05	0.08 ± 0.02	
Mean Total Annual Volume (km^3)	0.060	0.059	0.067	0.065	0.057	0.051	0.060 ± 0.006	
Max Total Annual Volume (km^3)	0.109	0.081	0.103	0.110	0.087	0.077	0.094 ± 0.015	
Mean Bankfull Volume (km^3)	0.027	0.034	0.037	0.033	0.027	0.024	0.031 ± 0.005	
Max Bankfull Volume (km^3)	0.074	0.047	0.072	0.073	0.050	0.031	0.058 ± 0.018	

	1955 - 1973	1973 - 1983	1983 - 1990	1990 - 2001	2001 - 2011	2011 - 2015	Totals
Duration (y)	18 ± 0.3	10 ± 0.3	7 ± 0.3	11 ± 0.3	10 ± 0.3	4 ± 0.3	
Area Eroded from SCREAM (m^2)	12228 ± 5060	12428 ± 2113	7341 ± 1835	16774 ± 2684	13317 ± 2530	3752 ± 1538	
Mean Depth of Eroded (m)	0.54 ± 0.01	0.60 ± 0.01	0.58 ± 0.01	0.69 ± 0.01	0.61 ± 0.01	0.72 ± 0.01	
Volume Eroded (m^3)	**-6640 ± 2751**	**-7476 ± 1277**	**-4272 ± 1071**	**-11519 ± 1851**	**-8080 ± 1541**	**-2713 ± 1113**	**-40700** ± 4169
Mean erosion rate (m^3/y)	-369 ± 153	-748 ± 130	-610 ± 155	-1047 ± 171	-808 ± 156	-678 ± 283	
Mean bank area erosion rate (m^2/y)[c]	#REF! ± #REF!	#REF! ± #REF!	#REF! ± #REF!	#REF! ± #REF!	#REF! ± #REF!	#REF! ± #REF!	
Point bar area of accretion from SCREAM (m^2)	28392 ± 4356	12391 ± 1735	14534 ± 2035	13612 ± 2178	14493 ± 1884	7403 ± 1851	
Mean vertical accretion within eroded areas (m)	0.59 ± 0.01	0.33 ± 0.01	0.23 ± 0.01	0.36 ± 0.01	0.33 ± 0.01	0.13 ± 0.01	
Estimated accretion along point bars (m^3)	16865 ± 2608	4089 ± 587	3357 ± 493	4941 ± 803	4783 ± 640	977 ± 255	
Overbank deposition from regression (m^3)	459 ± 92	302 ± 61	213 ± 44	305 ± 62	322 ± 66	168 ± 36	
Total volume accreted (m^3)	**17324 ± 2610**	**4391 ± 590**	**3570 ± 495**	**5246 ± 806**	**5105 ± 643**	**1145 ± 258**	**36780** ± 2921
Mean accretion rate (m^3/y)	962.43 ± 145.87	439.11 ± 60.462	509.97 ± 73.961	476.9 ± 74.406	510.54 ± 66.126	286.16 ± 67.924	
Net volume (m^3)	**10684 ± 3792**	**-3085 ± 1407**	**-702 ± 1179**	**-6273 ± 2018**	**-2975 ± 1670**	**-1568 ± 1142**	**-3920 ± 5091**

Figure 1.

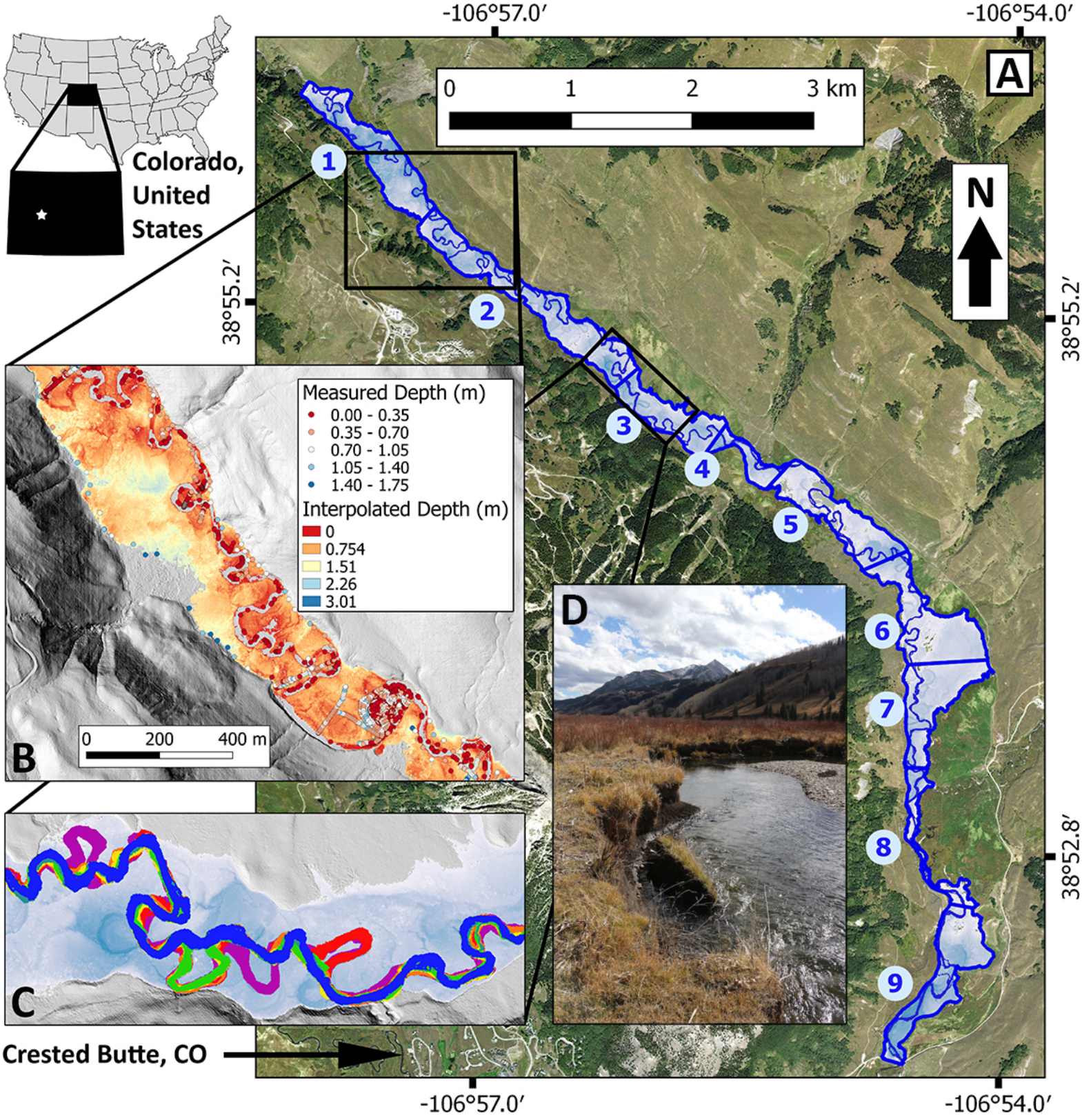
-106°57.0′
-106°54.0′
38°55.2′
38°52.8′
A
0 1 2 3 km
N
1
2
3
4
5
6
7
8
9
Colorado, United States
Measured Depth (m)
0.00 - 0.35
0.35 - 0.70
0.70 - 1.05
1.05 - 1.40
1.40 - 1.75
Interpolated Depth (m)
0
0.754
1.51
2.26
3.01
B
0 200 400 m
C
D
Crested Butte, CO

Figure 2.

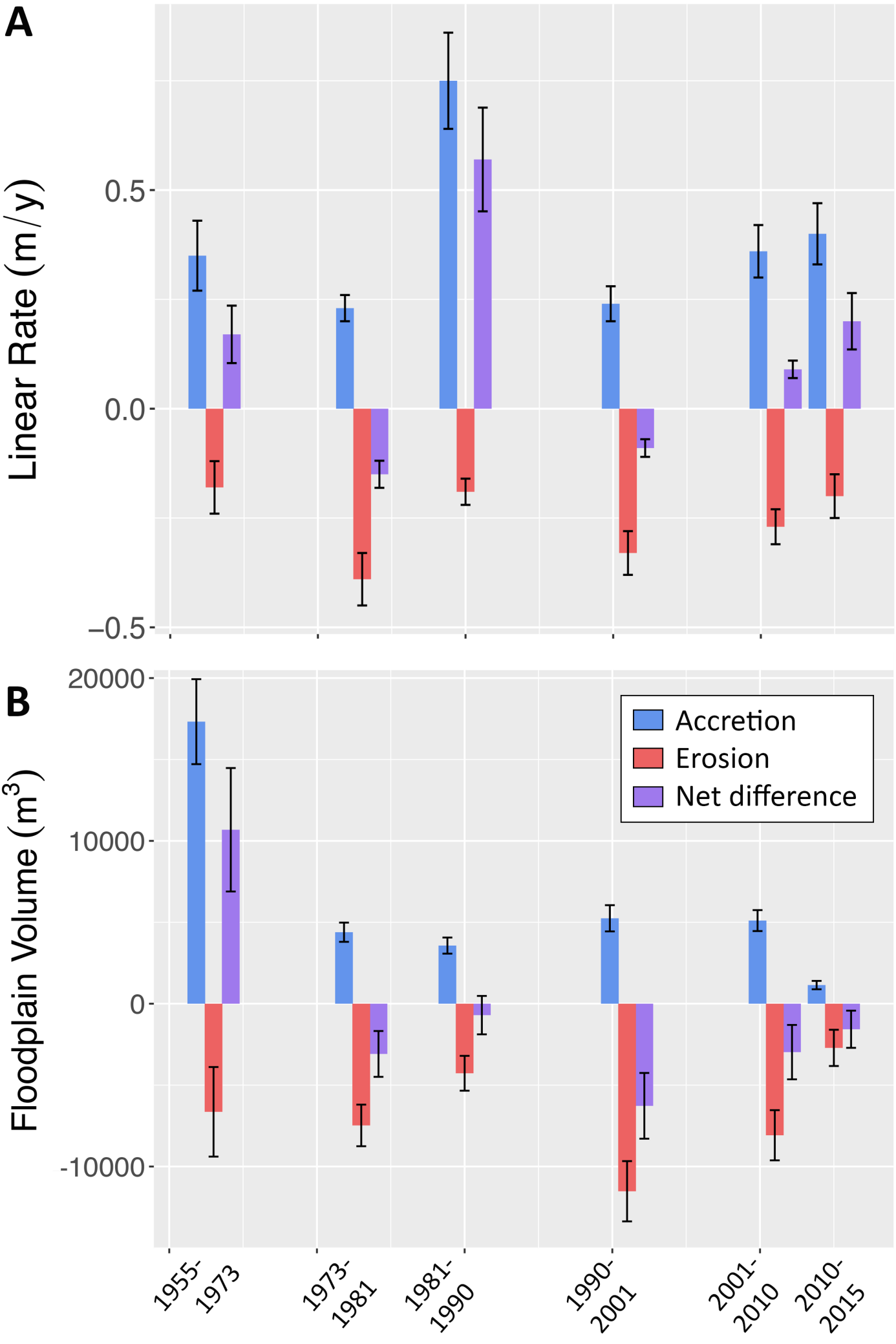
A
Linear Rate (m/y)
0.5
0.0
–0.5
B
Floodplain Volume (m3)
20000
10000
0
-10000
Accretion
Erosion
Net difference
1955-1973
1973-1981
1981-1990
1990-2001
2001-2010
2010-2015

Figure 3.

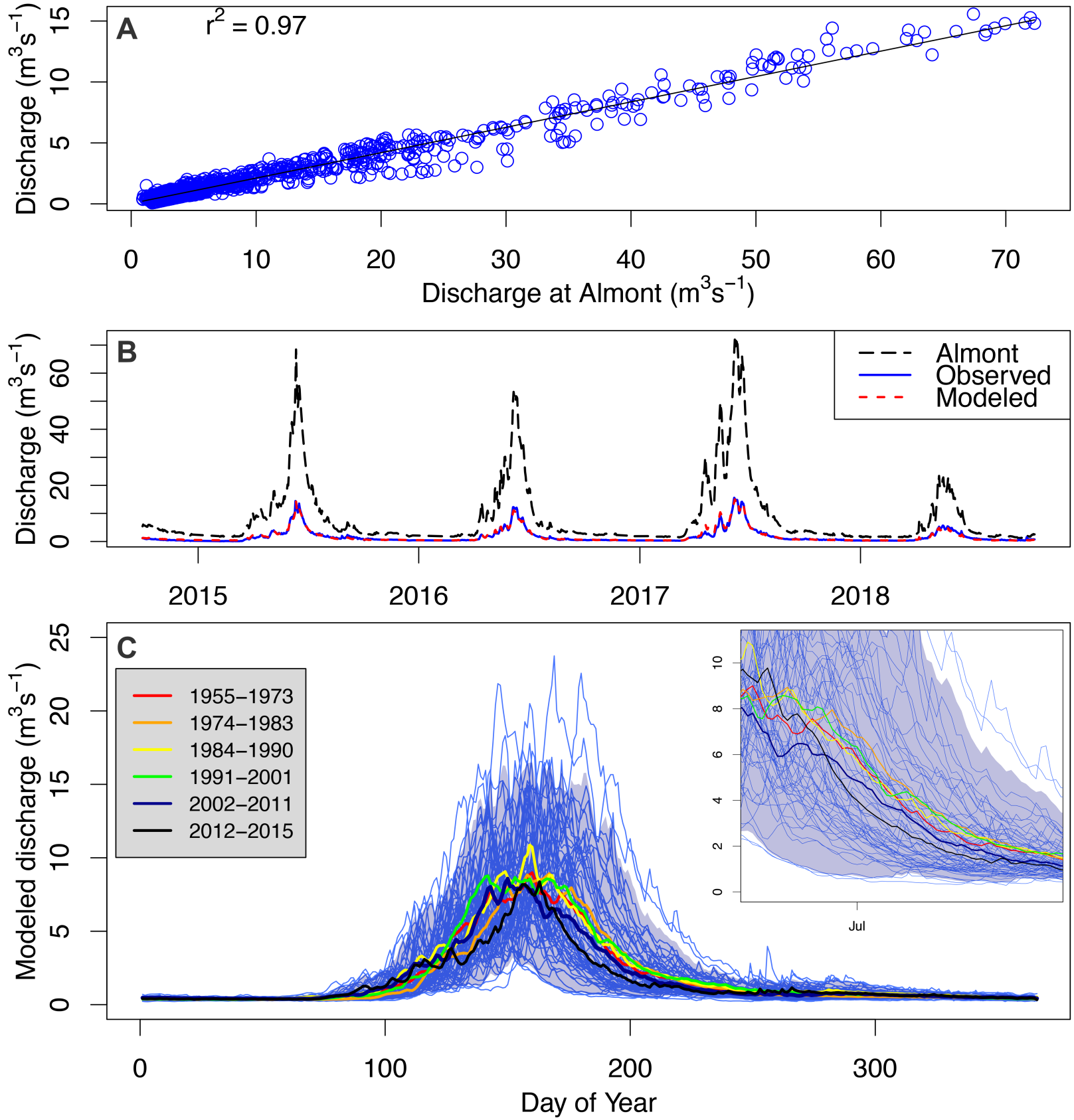
A
r^2 = 0.97
Discharge (m^3s^{-1})
0
5
10
15
0
10
20
30
40
50
60
70
Discharge at Almont (m^3s^{-1})
B
Almont
Observed
Modeled
Discharge (m^3s^{-1})
0
20
40
60
2015
2016
2017
2018
C
1955–1973
1974–1983
1984–1990
1991–2001
2002–2011
2012–2015
Modeled discharge (m^3s^{-1})
0
5
10
15
20
25
0
100
200
300
Day of Year
0
2
4
6
8
10
Jul

Figure 4.

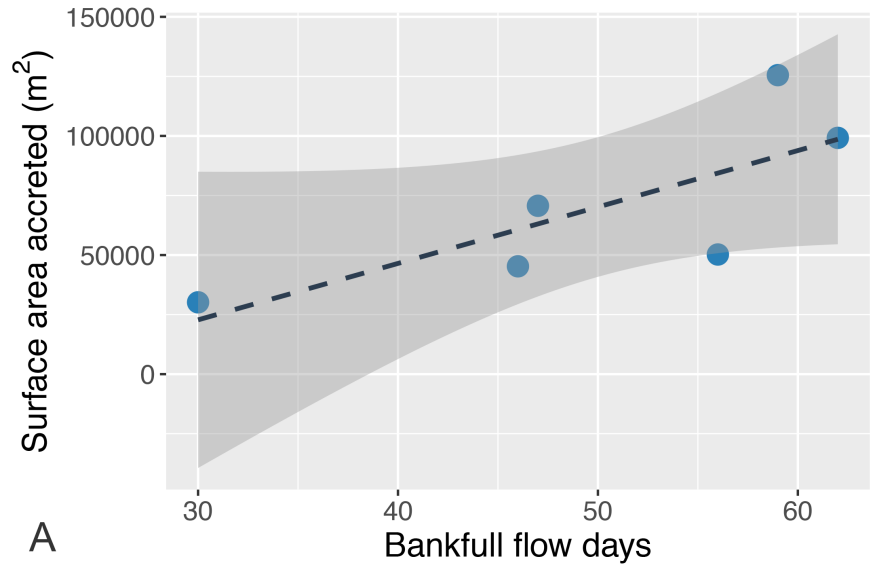
Surface area accreted (m2)
150000
100000
50000
0
30
40
50
60
Bankfull flow days
A

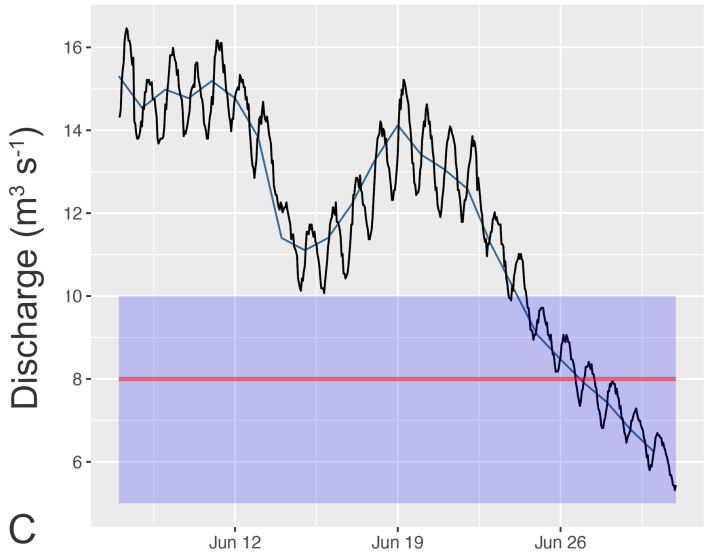
Discharge (m3 s-1)
16
14
12
10
8
6
Jun 12
Jun 19
Jun 26
C

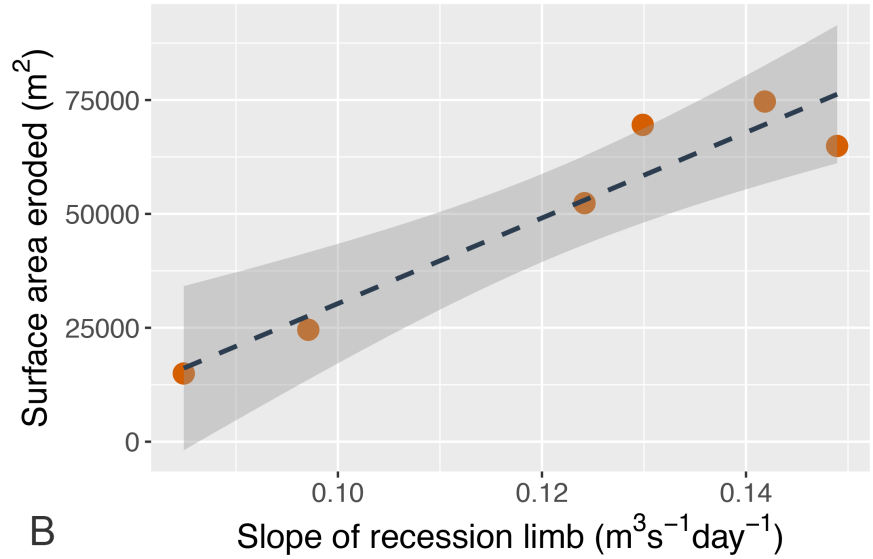
Surface area eroded (m2)
75000
50000
25000
0
0.10
0.12
0.14
Slope of recession limb (m3s−1day−1)
B

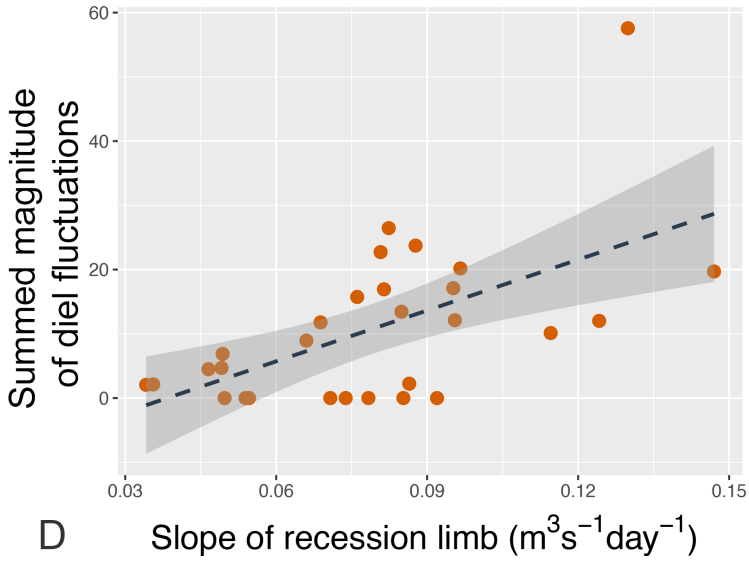
Summed magnitude of diel fluctuations
60
40
20
0
0.03
0.06
0.09
0.12
0.15
Slope of recession limb (m3s−1day−1)
D